

國立交通大學

光電工程研究所 碩士論文

飛秒雷射技術與其在非線性顯微術上的應用

Femtosecond Pulse Shaping Methodology and its
Applications in Nonlinear Optical Microscopy



研究生：陳明彰

指導教授：黃中堯

中華民國九十三年六月

飛秒雷射技術與其在非線性顯微 術上的應用

研究生：陳明彰

指導教授：黃中堯

國立交通大學研究所

摘要



本論文主要是研究控制和量測飛秒賣衝。在控制上，我們用 Gerchberg-Saxton 演算法，來設計飛秒賣衝波形。在量測方面，我們提出一個新的演算法，得以精確量測賣衝。在實驗和模擬上這個新的演算法都比傳統的基因演算法快、更精確、更能抵抗雜訊的影響，我們運用此演算法探測三種不同的半導體飽和吸收反射鏡。我們也運用此技術到非線性顯微術上。

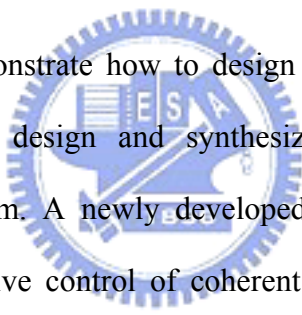
Femtosecond Pulse Shaping Methodology and its Applications in Nonlinear Optical Microscopy

Student: Ming-Chang Chen

Advisor: Professor Jung Y. Huang

Institute of Electro-Optical Engineering National Chiao Tung University

Abstract



In this thesis we demonstrate how to design and measure optical pulses. We demonstrate how to design and synthesize optical pulses by using Gerchberg-Saxton algorithm. A newly developed phase-freezing scheme for characterization and adaptive control of coherent optical pulses is described. The operational principle is based upon the concept that the highest peak intensity shall correspond to a complete frozen-phase state of all spectral components involved in a coherent optical pulse. Our experimental and theoretical results reveal this new scheme to be faster, accurate and more immune to the noise and laser power fluctuation than that with genetic algorithm. This freezing phase scheme had been employed for investigating three types of semiconductor saturable absorber Bragg reflectors (SBR) and the influence on the spectral phase distortion with subtle change of device structure was revealed. The application of the new phase freezing scheme on nonlinear optical microscopy is also presented.

誌謝

在碩士研究生涯中，首先我要特別感謝我的指導教授 黃中堯博士給我的指導與鼓勵，提供良好的的學習環境，在研究方向上及待人處世的態度方面讓我受益良多，每次遭遇研究瓶頸，他那鍥而不捨、突破困難的精神，著實令我難忘。

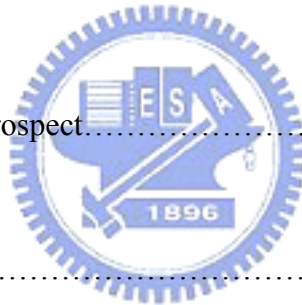
其次，非常感謝我的父母及家人，因為他們的愛與支持，讓我無後顧之憂的悠游於學海之中；每當我遭遇困難時，他們總是以最大的耐心聽我傾訴並給我鼓勵，今日我能有此成就完完全全要歸功於他們。

在研究過程中遇到的一些問題，在此要感謝楊乾鎖博士、李義民博士、李兆達博士，給予我啟發性的指導。同時，要感謝潘晴如、陳琬琪、施文慈學姐、蔡亦彥、陳立志、郭怡君學弟妹的幫忙，大家的參與讓我擁有這段多采多姿的日子。

CONTENTS

1. Introduction	1
2. Synthesis of Femtosecond Optical Pulses.....	4
2.1 Cr ⁴⁺ :Forsterite Femtosecond Laser System.....	4
2.2 All-Reflective Pulse Shaping Apparatus.....	5
2.3 Synthesis of Femtosecond Optical Pulses with Gerchberg-Saxton Algorithm	
2.3.1 Brief Description of Gerchberg-Saxton Algorithm.....	7
2.3.2 Simulation of the Optical Synthesis Procedure.....	8
2.3.3 Experimental Results of Optical Synthesis of Femtosecond Optical Pulses	
.....	12
3. Complete-Field Characterization with Freezing Phase Scheme.....	14
3.1 THEORETICAL BACKGROUND.....	15
3.2 Experimental Details.....	17
3.3 RESULTS.....	18
A. Simulation.....	18
A.1 Freezing procedure with a left-to-right scan scheme.....	20
A.2 Freezing procedure with a center-to-two sides scan scheme.....	21
A.3 Freezing procedure with a cascading thinning-out scheme.....	22
A.4 Noise influences on various freezing phase schemes.....	24
B. Experimental Results and Discussion.....	25
B.1 Phase retrieving from phase-sensitive second-harmonic patterns.....	25

<i>B.2 Complete-field characterization of semiconductor saturable absorber mirrors with an adaptive control pulse shaper</i>	26
<i>B.3 Comparison to genetic algorithm</i>	32
4. Coherent Control Nonlinear Optical Microscopy.....	34
4.1 Experimental Description.....	34
4.2 SHG as the Adaptive Coherent Control Signal.....	36
4.3 Two-Photon-Excited Fluorescence as the Adaptive Coherent Control Signal...40	
A. <i>Explanation of the measured coherent control phase profiles</i>	41
4.4 Coherent Control Tomography.....	42
5. Conclusion and Future Prospect.....	45
References.....	47



LIST OF FIGURES

2.1	<i>Left:</i> Optical schematic of Cr ⁴⁺ :Forsterite laser system. <i>Right:</i> The spectrum of the ultra short optical pulses generated from the Cr ⁴⁺ :Forsterite laser.....	5
2.2	Schematic and real setup of our phase-only pulse shaper.....	5
2.3	Schematic of the Gergberg-Saxton algorithm employed for retrieval of the spectral phase of the electric field desired.....	7
2.4	Simulated results to demonstrate the optical synthesis of femtosecond optical pulses with GSA.....	12
2.5	corresponding intensity autocorrelation curves obtained by integrating the FROG traces over the time axis.....	13
3.1	corresponding intensity autocorrelation curves obtained by integrating the FROG traces over the time axis.....	17
3.2	Schematic of the adaptive coherent control system with an all reflective 4- <i>f</i> pulse shaper used in this study.....	18
3.3	Flow chart depicts the procedure used to implement the freezing-phase scheme into the theoretical and experimental studies...	19

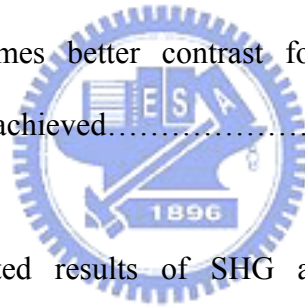
3.4	(a) Time course of the maximum SH intensity during the phase-freezing procedure with a left-to-right scan scheme; (b) the intensity profiles of transform-limited pulse (TLP), phase-distorted input pulse (DP), and phase-compensated pulse after first, second, and third freezing phase scans; (c) the spectral phase profile of the input pulse (open circles), compensating phase profile (crosses), and error phase profiles after first (thin solid curve), second (short dashed), and third (thick solid curve) freezing phase scans.....	20
3.5	Time course of the maximum SH intensity during the freezing phase procedure with a center-to-two sides scan scheme; (b) the intensity profiles of transform-limited pulse (TLP), phase-distorted input pulse (DP), and phase-compensated pulse after first, second, and third freezing phase scans; (c) the spectral phase profile of the input pulse (open circles), compensating phase profile (crosses), and error phase profiles after first (thin solid curve), and second (short dashed) freezing phase scans.....	22
3.6	Time course of the maximum SH intensity during the freezing phase procedure with a cascading thinning-out scheme; (b) the intensity profiles of transform-limited pulse (TLP), phase-distorted input pulse (DP), and phase-compensated pulse after first, second, and third freezing phase scans; (c) the spectral phase profile of the input pulse (open circles), compensating phase profile (crosses), and error phase	

profiles after 8s (short dashed), 32s (dotted), and 128s (thick solid curve) freezing phase scans.....	23
3.7 Time courses of SH signal as a function of the number of freezing steps with a variety of freezing procedures: cascading thinning-out scheme (solid curve), a center-to-two sides scan scheme (long-dashed curve), and left-to-right scan scheme (short-dashed line).....	25
3.8 Dependence of the measured SHG intensity of an optical pulse reflected from a gold-coated mirror on the phase retardance of three consecutive pixels of SLM.....	26
3.9 Calculated field distribution (with blue-red color coding) is presented with the device structure of saturable absorber Bragg reflectors with InAs-QD or <i>d</i> -QW embedded in a (a) $\lambda/4$ -thick layer or (b) $\lambda/2$ -thick layer.....	28
3.10 (a) Measured and (b) retrieved SHG-FROG patterns of femtosecond optical field at 1.25 μm reflected from the QD- $\lambda/2$ SBR and (c) the retrieved spectral phase profiles from <i>d</i> -QW (solid curve), QD- $\lambda/4$ (long dashed) and QD- $\lambda/2$ (short dashed line) SHG-FROG traces.....	28
3.11 (a) Spectral profiles of optical pulses reflected from <i>d</i> -QW (open circles) measured with freezing-phase algorithm (FA) and from <i>d</i> -QW (solid curve), QD- $\lambda/4$ (long dashed), QD- $\lambda/2$ (short dashed) with	

Fourier-transformed infrared spectroscopy (FTIR) (b) Spectral phase profiles from Au-mirror (thin solid curve), <i>d</i> -QW (thick solid curve), InAs QD- $\lambda/4$ (long dashed), and InAs QD- $\lambda/2$ (short dashed) deduced with phase freezing scheme; (c) group delay time of the three SBR devices over the entire pulse spectral range.....	30
3.12 Measured SHG is plotted as a function of the number of phase adjustments with the freezing phase algorithm (FA: blue solid curve) and genetic algorithm (GA: red-colored).....	32
4.1 Schematic arrangement for multiphoton microscopy. The pulse goes through the pulse shaper and tight focused by a $50\times/0.55$ NA objective. Intensities at the focal point can easily reach 10^{13} W/cm ²	35
4.2 Right: InAs self-assembled quantum-dot layer embedded in a half wave layer of GaAs on a DBR structure. The DBR stack is formed with 25 pairs GaAs/AlAs designed to yield a Bragg wavelength at $\lambda_B=1.23$ μm . The focal point of the NLO microscope objective lens is positioned to under the surface of the sample. Therefore optical pulses must penetrate a distance about 50 μm , before reach the focal point. The area labeled by ‘P’ displays some epi-defects on the surface. Other normal area is labeled by ‘S’. Left : Energy-level diagram of a resonant TPA in semiconductor saturable absorber. The pulse spectrum is centered on the two-photo transition frequency (1ω) at 1250 nm, with the bandwidth of 39 nm (FWHM). The frequency of SHG (2ω)	

corresponds to 625 nm. The frequency of the $1\omega'$ resonant transition corresponds to 868 nm..... 36

4.3 **Left:** The phase profile (green solid line) and spectral sensitivity plot of SHG (green dashed line) obtained by freezing phase algorithm. **Right:** Two images with $40\ \mu\text{m}\times 30\ \mu\text{m}$ taken from the same area of QD- $\lambda/2$ semiconductor saturable absorber mirror. The first image is measured with ultrashort pulses by taking all SLM-128 pixels to have zero phase retardation, and the second image is taken with a optimum coherent control phase pattern used for compensating the phase distortions from laser optics, objective lens, and the surface layer of the sample. Three times better contrast for two-photon excited fluorescent image was achieved..... 38



4.4 **Left :** Some simulated results of SHG and THG without an intermediate resonant energy level. The material is assumed to be excited by an ultrashort pulse with two different periodic phase modulation patterns. **Right :** Measured results of the QD- $\lambda/2$ InAs SBR with those two periodic phase modulation patterns..... 39

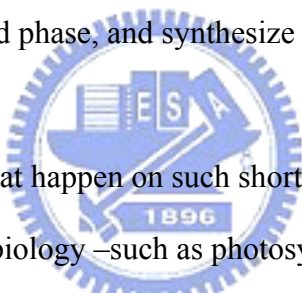
4.5 **Left:** Two-photon-excited fluorescent (TPF) spectral sensitivity (dash line) and phase retardation pattern (solid line) used to yield maximum TPF signal from position P (blue) and S (red). **Right:** The phase patterns [P'] and [S'] can generate higher TPF from position P and S, respectively..... 41

4.6 Two TPF scans on a $70 \times 60 \mu\text{m}$ region of the semiconductor saturable absorber mirror. **Top left:** TPF image at 868 nm taken with coherent control phase pattern [P']. **Top right:** TPF image at 868 nm taken with coherent control phase pattern [S']. **Bottom left:** coherent control TPF difference map resulted from subtracting those two TPF intensity distributions. **Bottom right:** TPF image at 886-nm with coherent control phase pattern [P']..... **43**



Chapter 1 Introduction

Optical coherent light pulses as short as a few femtoseconds (1 femtosecond = 1 fs = 1×10^{-15} sec) have been generated, and it currently becomes a routine work to generate sub 100-fs optical pulses. The recent unification of phase control of ultrawide-bandwidth laser with ultrafast laser technology has enabled the precise generation of optical frequency combs [6-18]. It is now possible to control the carrier-envelope phase of ultrafast pulses. It appears to have all the experimental techniques in hand for complete control over coherent light-matter interaction. These tools include the ability to generate coherent optical pulses with arbitrary shape, precisely control frequency and phase, and synthesize coherent light from multiple sources, *etc.*



Numerous phenomena that happen on such short time scales are important to study. Some key processes in biology –such as photosynthesis, vision transduction, protein-folding, *etc.* – contain events that occur on fs time scale. Crucial processes in chemistry – such as molecular vibrations, re-orientations, and collisions in condensed-phase – also occur on this time scale. Several important events in physics and engineering—such as high-lying excited-state lifetimes, photo-ionization, and photo-excited electron-hole relaxation in optical detectors and optoelectronics – are very fast too. Therefore to probe more deeply into the ultrafast light-matter interaction with a more controllable way is an important step toward an effective design and control of advanced materials and devices.

To achieve the goal, first we have to prepare a light pulse which is shorter than the event that we want to analyze. In general, any optical measurement of a medium or a device is ultimately limited by our ability to measure and control the light into

and out of the medium being studied. Complete-field characterization methods for optical pulse diagnosis can be categorized into two different types: Frequency-resolved optical gating (FROG), sonogram, and spectral phase interferometry for direct electric-field reconstruction (SPIDER), *etc.* belong to the first category. They can measure but can't compensate the ultrafast pulses involved. The second class of pulse characterization methods involves a pulse shaper, a nonlinear detection method and global optimization algorithm. This approach is capable of doing both pulse characterization and compensation simultaneously. This capability is extremely useful and can be incorporated into the ultrafast laser system being used.

This thesis presents theoretical and experimental studies on the design, characterization, and adaptive coherent control of ultrafast optical pulses. The application of the methodology on nonlinear optical microscopy is also given. This thesis is organized as follows: Chapter 2 shows our experimental setup of the laser system and femtosecond pulse shaping apparatus. Some critical procedures for aligning the pulse shaper are briefly described. We also demonstrate how to design and synthesize optical pulses by using Gerchberg-Saxton algorithm. Simulated and experimental results are shown for comparison. Concepts about how to improve this method and related discussion are offered.

In Chapter 3, we describe first a newly developed phase-freezing scheme. Some simulated results are presented in order to design a better phase compensation scheme with high immunity to noise. Applications of the method on several types of saturable Bragg reflector (SBR) devices are shown and finally discussion is offered.

In Chapter 4, application of the new phase freezing scheme on nonlinear optical microscopy is presented. We applied our apparatus for complete-field characterization and compensation for phase distortion from laser optics, microscope objective, and sample surfaces. One of the major concerns in this chapter is to find out the relation

between the absorption and spectral sensitivity. The influence of an intermediate level on the coherent-control nonlinear optical microscopy is also discussed. Finally, the conclusion and discussion are made.



Chapter 2 Synthesis of Femtosecond Optical Pulses

In this chapter, we shall introduce our laser system and phase-only pulse shaping apparatus. A Cr^{4+} :Forsterite femtosecond laser is first described in Section 2.1. The phase-only pulse shaping apparatus and some critical procedures for aligning the pulse shaper will be presented in Section 2.2. Some application examples of the setup for synthesis of femtosecond optical pulses with Gerchberg-Saxton algorithm are shown in section 2.3.

2.1 Cr^{4+} :Forsterite Femtosecond Laser System

The schematic of a Cr^{4+} :Forsterite femtosecond laser system from Avesta Project Ltd. (<http://www.avesta.ru>), which can generate ultrashort optical pulses in near infrared ($\lambda \sim 1250$ nm), is shown in Figure 2.1. The laser is self mode-locked by keeping lasing longitudinal cavity modes in phase to produce ultrashort near transform-limited optical pulses with pulse duration about 50 fs. The Cr^{4+} :Forsterite oscillator gives pulses with a typical full-width-at-half maximum (FWHM) bandwidth of about 45 nm at a repetition rate of 76 MHz and average power 270mW. The ultrashort pulse duration can yield an enormous peak power density after focusing. The Cr^{4+} :Forsterite laser is pumped by a 7.8-W Ytterbium-doped fiber laser.

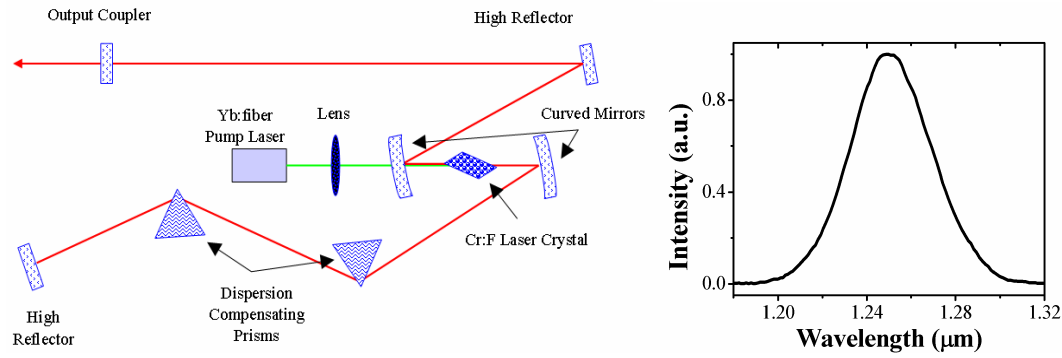


Fig 2.1: *Left:* Optical schematic of Cr⁴⁺:Forsterite laser system. *Right:* The spectrum of the ultra short optical pulses generated from the Cr⁴⁺:Forsterite laser

2.2 All-Reflective Pulse Shaping Apparatus

Our phase-only pulse shaper follows the design of 4-*f* dispersionless configuration, which consists of a pair of gratings (600 grooves/mm), two spherical reflectors with a focal length of $f=10$ cm, and a liquid crystal spatial light modulator (SLM, Cambridge Research and Instrumentation Inc. (CRI) Woburn, MA, SLM-128). The SLM consists of 128 2-mm-high phase-modulating elements with 97-μm width, and a 3-μm gap between adjacent pixels.

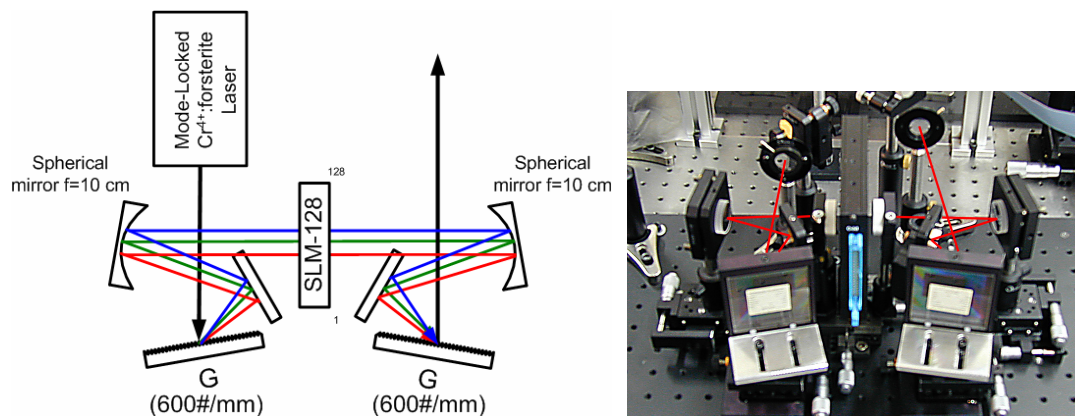


Fig 2.2: Schematic and real setup of our phase-only pulse shaper

To achieve minimum aberration and a dispersionless condition, properly aligned the apparatus is required. We devise an effective procedure to ensure that such conditions

have been met. The critical alignment steps are depicted in the following:

1. First let the laser beam go through a BBO crystal to generate a visible second-harmonic beam at 628 nm.
2. Adjusting the red input beam to propagate on a horizontal plane which is parallel to the optical table.
3. Checking out all the diffraction beams propagate on the horizontal plane. The broadband optical spectral components should also spread on the plane.
4. Place the first spherical mirror at approximately one focal length away from the first grating. Rotate the first grating to let the second-order diffracted beam to be centered on the spherical mirror.
5. Make sure that the image is on the SLM plane and all spreading optical spectral components still propagate on the horizontal plane.
6. Position the second spherical mirror at a distance of $2f$ from the first spherical mirror. Adjusting the angle of the second spherical mirror to let all spectral components approximately overlapped on the center of the second grating. Be sure that all beams still propagate on the horizontal plane.
7. Fine tuning the position and the angle of the second grating to let all diffracted spectral components collimate. One can put a mask on the SLM plane and just let two spectral components pass through. This two components will cross on the grating by adjusting the position of G' , and let the diffracted components into the same direction by adjusting the angle of G' .
8. Finely adjusting the distance between the two spherical mirrors to optimize the output spot for as circular as possible. Make sure the distance between these two spherical mirrors to be $2f$. The output spot shall look like circular in far field.
9. Repeat step 7 and 8 until a circular spot in the far field is obtained.
10. Place SLM at approximately the image plane of the first spherical mirror where

individual spectral components are focused to their minimum size.

2.3 Synthesis of Femtosecond Optical Pulses with Gerchberg-Saxton Algorithm

In this section, we shall demonstrate synthesis of femtosecond optical pulse with arbitrary pulse profile by using Gerchberg-Saxton algorithm (GSA).

2.3.1 Brief Description of Gerchberg-Saxton Algorithm

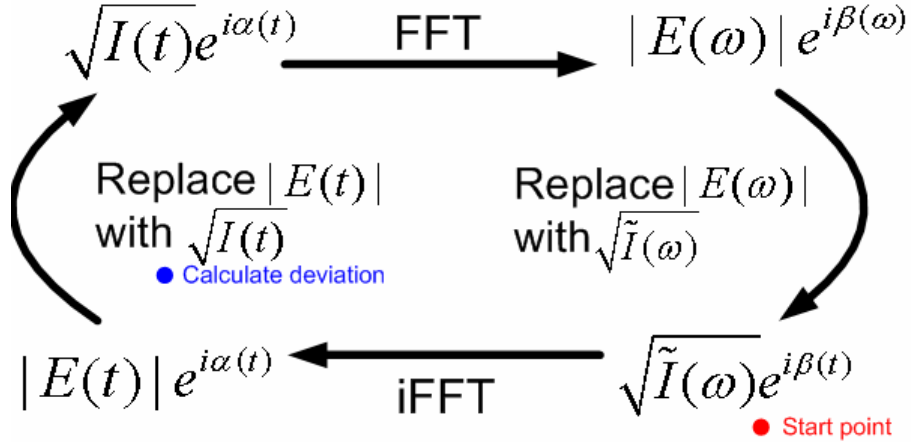


Fig 2.3: Schematic of the Gerchberg-Saxton algorithm employed for retrieval of the spectral phase of the electric field desired. The red point denotes the starting point of the algorithm and the blue spot indicates the monitoring point for the deviation between the target pulse $\{\sqrt{I(t)}\}$ and the temporal pulse $\{|E(t)|\}$ at this moment.

In literature, GSA had been used for recovering two-dimensional spatial phase information of images when only the amplitude of the optical field is available at near and far-field planes [23, 24, 25]. Fig. 2.3 displays a flow chart of the procedure, where $\{\sqrt{\tilde{I}(\omega)}\}$ denotes the available spectral amplitude, $\{|E(\omega)|\}$ is the amplitude of the field, $\{\sqrt{I(t)}\}$ is the amplitude of the target pulse, $\{|E(t)|\}$ is the temporal field

profile, and $\{\beta(\omega)\}$ is the spectral phase needed for producing the desired target pulse from an input pulse.

The pulse synthesis procedure starts with transforming a trial electric field to the frequency domain. We replace the resulting $\{|E(\omega)|\}$ by $\{\sqrt{\tilde{I}(\omega)}\}$ (the measured spectrum of the input pulse) while leaving the phase unaltered. Then the field is transformed back to the time domain and replaces $\{|E(t)|\}$ with $\{\sqrt{I(t)}\}$ while leaving the phase unaltered. The procedure is repeated until the deviation between the amplitude of the desired pulse $\{\sqrt{I(t)}\}$ and temporary field $\{|E(t)|\}$ as small as possible. Usually, the whole procedure can be achieved within about 20 iterations to yield the desired spectral phase profile $\{\beta(\omega)\}$. By using the algorithm we determine the spectral phase pattern needed by the SLM (128-pixel 1D LC array) for producing the target pulse $\{\sqrt{I(t)}\}$.



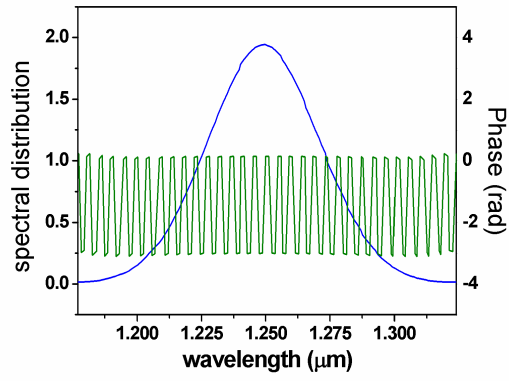
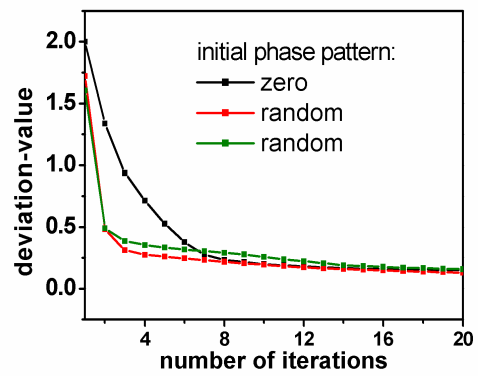
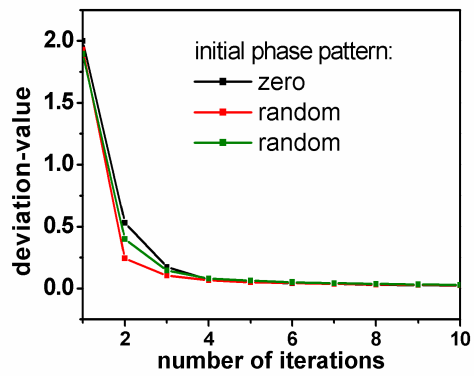
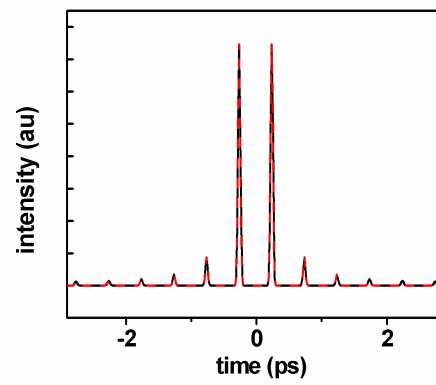
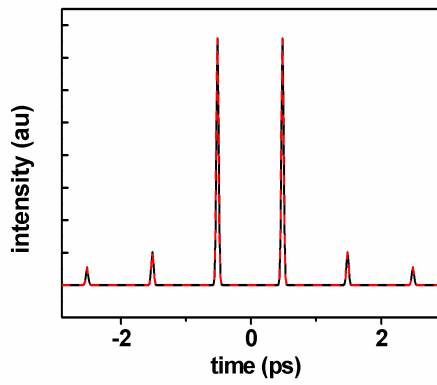
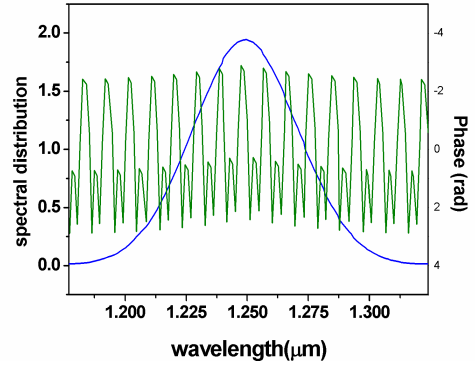
2.3.2 Simulation of the Optical Synthesis Procedure

To successfully implement the algorithm, first we have to measure the spectrum of the input laser pulse ($\sqrt{\tilde{I}(\omega)}$). To synthesize the desired pulse we express the target pulse profile $I(t)$ on a FFT grid, which corresponds to the number of the SLM elements. We start the algorithm at the position marked by red spot in Fig. 2.3. A trial electric field with a spectral amplitude being the square root of the measured spectrum $\{\sqrt{\tilde{I}(\omega)}\}$ and an initial spectral phase $\{\beta(\omega)\}$ being either constant or random noise distribution is used. We then launch the algorithm until the deviation between the amplitude of the target pulse ($\sqrt{I(t)}$) and the temporary field ($|E(t)|$) estimated at the blue spot in Fig. 2.3 is less than an error upper limit. We can also

implement a proper error checking criterion to automate the procedure.

Four examples are presented in Figure 2.4. Examples shown in Figure 2.4(a) and 2.4(b) are aimed to demonstrate how to precisely synthesize periodic pulses from a single input pulse. Note that only spectral phase modulation is used to achieve the goal. The other two examples are used to test whether GS algorithm is capable of finding the spectral phase pattern required for generating a specified waveform.

The first row of the Figure 2.4 shows the available spectral amplitude $\{\sqrt{\tilde{I}(\omega)}\}$ in blue-colored curve and the desired spectral phase $\{\beta(\omega)\}$ shown by the green curve. The second row presents the temporal intensity profile of the target pulse (red-colored line) and the best output pulse (black line). In the third row, the root-mean-squared (RMS) deviation of the best temporal profile from the target profile is shown as a function of iterations, which indicates that a satisfactory result can be obtained with only 10 to 20 iterations. The initial random phase pattern yields an optimal result faster than that with a constant phase pattern [24]. Although the exact number of iterations depends on the initial phase pattern, the algorithm converges to the same solution in all cases being studied.

a**b**

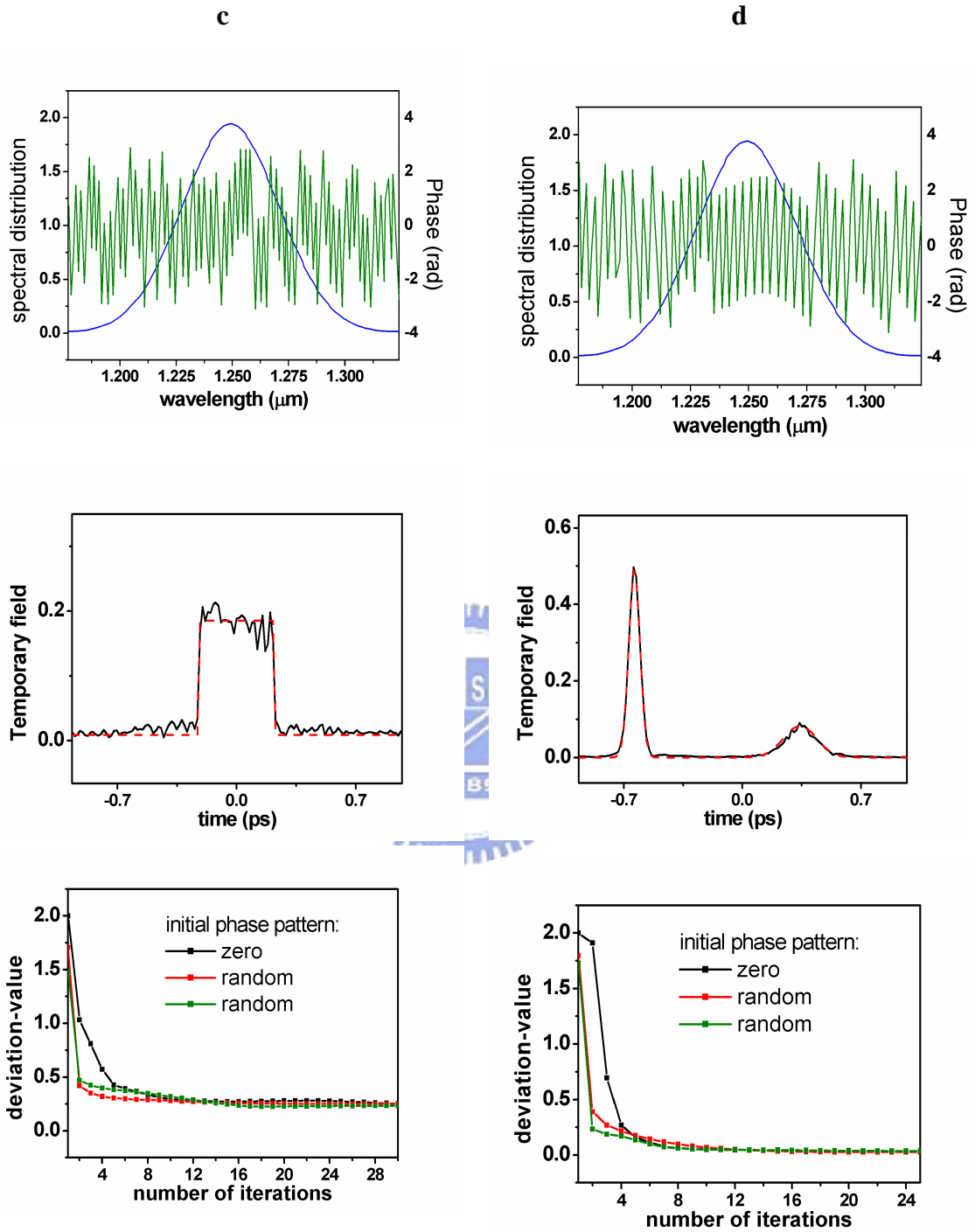


Fig 2.4: Simulated results to demonstrate the optical synthesis of femtosecond optical pulses with GSA. The first figure row shows the spectrum of the input pulse (blue-colored line) and the spectral phase profile (green line) needed for generating the target pulse. The second row presents the comparison of the resulting output pulse profile from pulse shaper (black line) and the target pulse (red line). The third row shows the root-mean-squared (RMS) deviation of the best result of temporal pulse profile from the target pulse as a function of iterations. The target pulses used are (a) pulses train separated by 1 ps; (b) pulses train separated by 0.5 ps; (c) 0.55-ps rectangular pulse; and (d) 200-fs pulse separated with an arbitrary pulse by 1-ps.

2.3.3 Experimental Results of Optical Synthesis of Femtosecond Optical Pulses

Experimental verification of the simulated results with GSA was carried out by using second-harmonic generation frequency-resolved optical gating (SHG-FROG) technique. The optical phase retardation patterns obtained from GSA were uploaded to our phase-only pulse shaper with an LC SLM-128 in the Fourier plane. The output pulse from the shaper is brought to a home-made SHG-FROG setup. When the optical phase retardation pattern of Figures 2.4(a) and 2.4(b) were uploaded to SLM128, the resulting FROG traces are presented in in the Figs. 2.5(a) and 2.5(b), respectively.

Some differences between simulated and experimental results may come from the actual spectral resolution of the SLM, the diffraction caused by SLM, and the non transform-limited pulses from laser. The results confirm that we can indeed synthesize femtosecond optical pulses with a specific period. However, if we want to synthesize optical pulse more accurately, we have to use a feedback signal to inform computer about the current status of the temporal pulse. Relying on this signal, computer could know how to improve the optical phase retardation pattern to approach the desired target pulse [8].

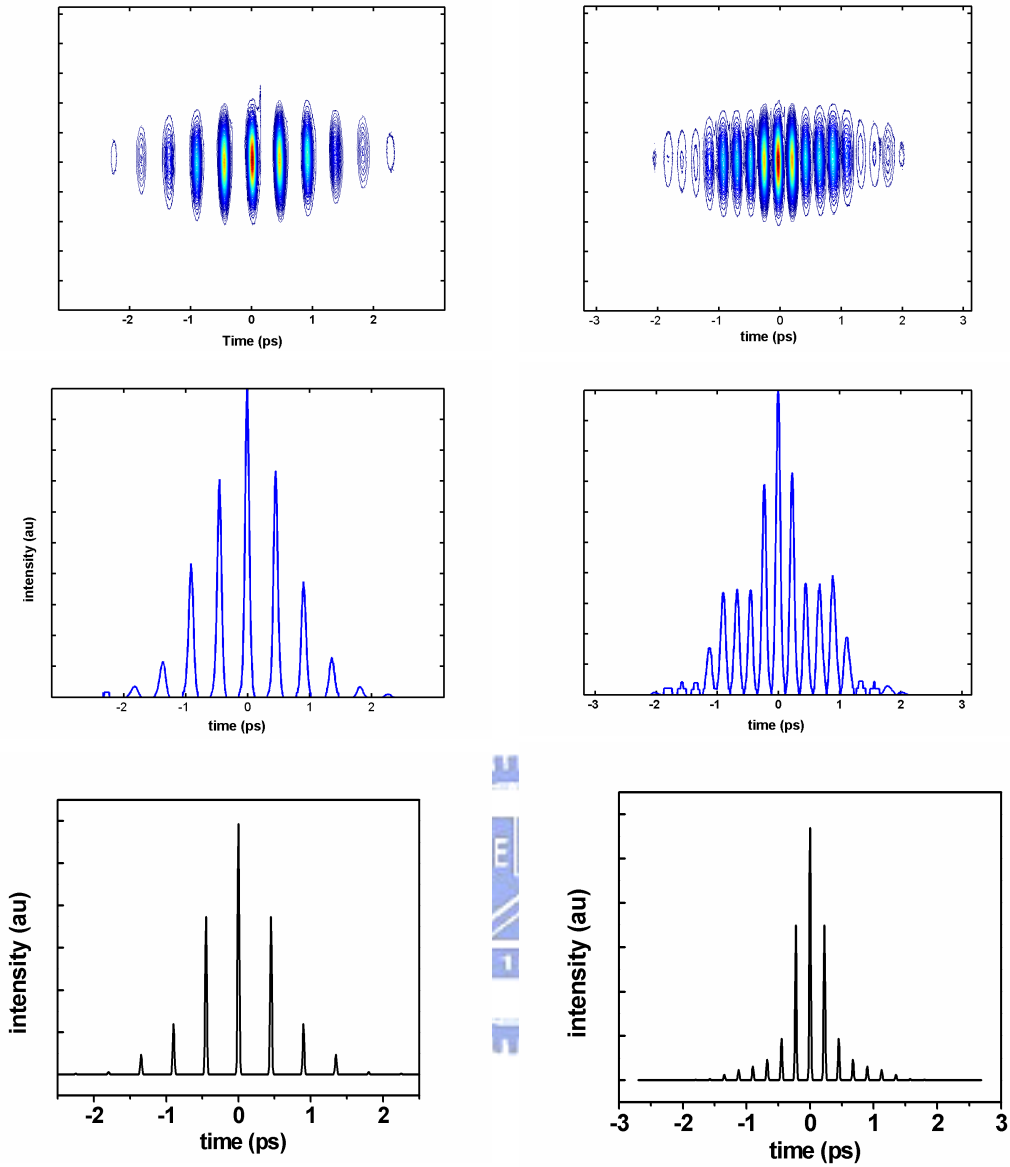


Fig 2.5: The first row shows the measured FROG traces of the output pulses from the pulse shaper with optical phase retardation patterns of Figs. 2.4(a) and 2.4(b). The second row shows the corresponding intensity autocorrelation curves obtained by integrating the FROG traces over the time axis. The third rows show the calculated autocorrelation curves of the electric fields with the optical phase retardation patterns of Figures 2.4(a) and 2.4(b).

Chapter 3 Complete-Field Characterization with Freezing Phase Scheme

In the quest to control and steer the quantum states of complex systems, an attractive scheme is adaptive laser pulses control, as first introduced by Judson and Rabitz [1]. An algorithm is employed to tailor a coherent optical field to prepare specific products on the basis of fitness information. The concept appears to be universal and several progresses have already been reported in literature [1-11].

By using the broadband property of an ultrashort laser pulse, Silberberg *et al.* had developed a coherent control scheme to demonstrate selective imaging of molecules with single-pulse coherent anti-Stokes Raman scattering [2]. Similar enhancement with coherent control technique was also observed in two-photon fluorescence process [3, 4]. Along this study, the question remained is whether the optimal laser field contains a set of rational rules that govern the dynamics. Recent study appears to reveal that the answer could be affirmative [5]. Therefore, the purpose of femtosecond coherent control study is not only to control the evolution of a complex system but also to deduce the detailed dynamic mechanism from the optimal laser field used.

Coherent control technology has been demonstrated with femtosecond optical pulses by using a pulse shaper with spatial light modulation devices [6-18]. The simplest approach of pulse shaping with conserved pulse energy is to adjust spectral phase for tailoring the pulse shape [6-11]. We can imagine the spectral phase components involved in a coherent pulse to be a system of interacting particles. If a temperature sensor to reveal how cold it is at zero degree and a thermal pump to control the amount of heat to be added into or taken from the system are available, information about the interacting-particles can be yielded by studying how the system

responses to a thermal excitation.

In this chapter, we implement this concept into a coherent control setup for yielding both functions of adaptive pulse shaping and characterization [4]. A spatial light modulator (SLM) plays the role of thermal pump and a phase-sensitive photon detector provides the thermal-sensing function. We note that to generate the highest second-harmonic signal from a transparent nonlinear optical crystal, all the spectral phase components of a coherent pulse shall be in-phase (hereafter this state is termed as frozen-phase state). We use SLM to manipulate the phases of the spectral components and adaptively reduce the deviation from the frozen-phase state with our new phase compensation scheme.

This chapter is organized as follows: in Section 3.1, we present the theoretical background of the new freezing phase scheme. Our experimental setup is then detailed in Section 3.2. We offer some simulation results in Section 3.3.A in order to develop an efficient phase compensation scheme with highest noise immunity. Finally experimental results of several types of SBR devices are presented and discussion is offered in Section 3.3.B.

3.1 THEORETICAL BACKGROUND

To verify the functionality of the freezing phase scheme, we first express optical field in terms of its spectral components in 128 elements:

$$E(t) = \sum_{n=-63}^{64} A_n \exp[j(\omega_0 + n \Delta\omega) t + \phi_n], \quad (3-1)$$

where $\Delta\omega$ is the width of spectral components involved in the coherent pulse, ϕ_n and A_n denote the phase constant and amplitude of each spectral component, and ω_0 is the optical carrier frequency.

In a typical 4- f pulse shaping setup, the pulse spectrum is angularly dispersed by

a grating [19]. The 128-pixels SLM can be used to impose a phase retardation pattern $\{\Theta_n\}$ on the optical spectrum and transforms the coherent field into a shaped field of

$$E(t) = \sum_{n=-63}^{64} B_n \exp[j(\omega_0 + n \Delta\omega) t + \phi_n + \Theta_n], \quad (3-2)$$

where the ratio of B_n / A_n denotes the field transmittance of the n th pixel. The phase constants $\phi_n + \Theta_n$ of all the spectral phasors must be identical to each other to produce the shortest pulse and therefore the highest peak intensity. Equation (3-2) indicates that the peak amplitude of the shaped field $E(t)$ can reach a maximum value when $\phi_n = -\Theta_n$.

We first note that two-beam interference can accurately yield the information of phase difference. In brief our algorithm can first divide the elements of SLM into two groups:

$$\begin{aligned} B_1 \exp(i\theta_1) &= \sum_{n=G_1} B_n \exp[j(\omega_0 + n \Delta\omega) t + \phi_n], \\ B_2 \exp(i\theta_2) &= \sum_{n=G_2} B_n \exp[j(\omega_0 + n \Delta\omega) t + \phi_n] \end{aligned}$$

By changing one phase and let the other interfere with each other. The second-harmonic (SH) signal generated from a nonlinear optical crystal with the optical coherent pulse can vary with

$$\begin{aligned} |E|^4 &= |B_1 \exp(i\theta_1) + B_2 \exp[i(\theta_2 + \Psi)]|^2 \\ &= \{|B_1|^2 + |B_2|^2 + |B_1| \times |B_2| \times \cos(\theta_1 + \theta_2 + \Psi)\}^2. \end{aligned}$$

We can freeze the phase Ψ to achieve the maximal SH signal by letting $\theta_1 = \theta_2 + \Psi$. In other words, SLM can be used to make those two spectral groups in-phase.

To further illustrate the freezing phase procedure, we use four phasors to represent the spectral phase profile of a coherent optical pulse. The optical field can therefore be simplified as $E(t) = \sum_{i=1}^4 v_i e^{i\phi_i}$. The distorted phase profile of the pulse in the complex field plane is shown in Fig. 3.1(a). To freeze the spectral phases, we first

pick up a spectral component and align the phasor with the summed direction of the rest spectral components by using SLM to introduce a compensation phase. Specifically, for example, we can combine $v_1e^{i\phi_1}, v_2e^{i\phi_2}$ and $v_3e^{i\phi_3}$ into the reference group and allow $v_4e^{i\phi_4}$ to vary (see Fig. 3.1(b)). The same procedure is repeated on $v_3e^{i\phi_3}, v_2e^{i\phi_2}$ and $v_1e^{i\phi_1}$ (Fig. 3.1(c) \rightarrow (e)). In Fig. 3.1(f) a final fine tuning is performed on $v_4e^{i\phi_4}$ again to achieve a frozen phase state.

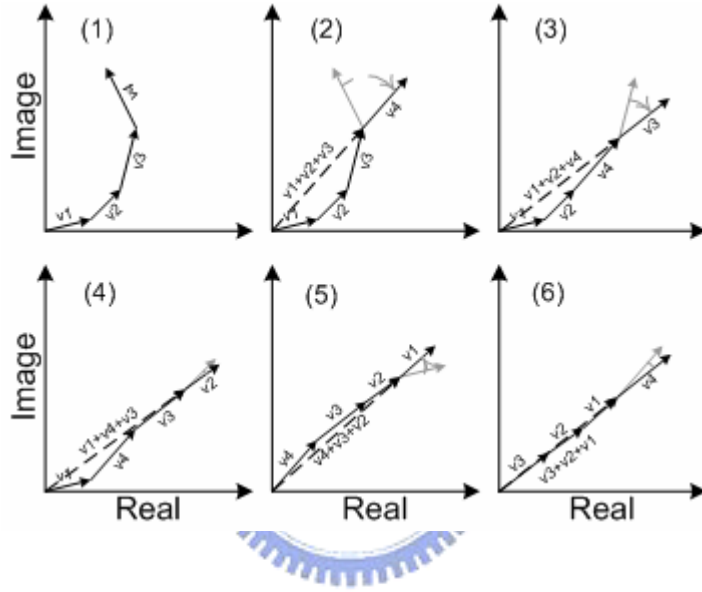


Fig. 3.1: (a \rightarrow f) corresponding intensity autocorrelation curves obtained by integrating the FROG traces over the time axis.

3.2 EXPERIMENTAL DETAILS

Figure 3.2 presents the schematic of an adaptive pulse shaping apparatus¹⁹ used in this study. The laser system is a Cr^{4+} : forsterite laser pumped by a diode-pumped Yb: fiber laser (IPG Photonics, Ltd.). A typical output of the Cr: forsterite laser was 280 mW of average power at a repetition rate of 76 MHz with a 7.5-W pump. The central wavelength is 1.252 μm , and a typical full-width-at-half maximum (FWHM) bandwidth was approximately 42 nm, corresponding to 50-fs pulse duration. All those experimental setup is mentioned as previous chapter.

The pulse is tailored by a pulse shaper consisting of a pair of gratings (600 g/mm), two concave reflectors with a focal length of $f=10$ cm, and a liquid crystal SLM (Cambridge Research and Instrumentation Inc. (CRI) Woburn, MA, SLM-128). The SLM consists of 128 97- μm -wide pixels, with a 3- μm gap between adjacent pixels. After reassembled by the output grating, the shaped pulse is focused onto a sample under test. The phase distortion in the reflected optical pulse can be pre-compensated by the SLM. An optical pulse with constant phase can therefore be yielded before a 3-mm thick type-I $\beta\text{-Ba}_2\text{BO}_4$ (BBO) second harmonic generation (SHG) crystal. Note that transform-limited pulse with constant phase can produce a maximum second-harmonic (SH) signal from a transparent nonlinear optical crystal. We therefore combine BBO SHG with a photodiode to offer a functionality of constant phase detection. The photodiode signal is sent to a computer for generating phase compensating pattern with the freezing-phase algorithm.

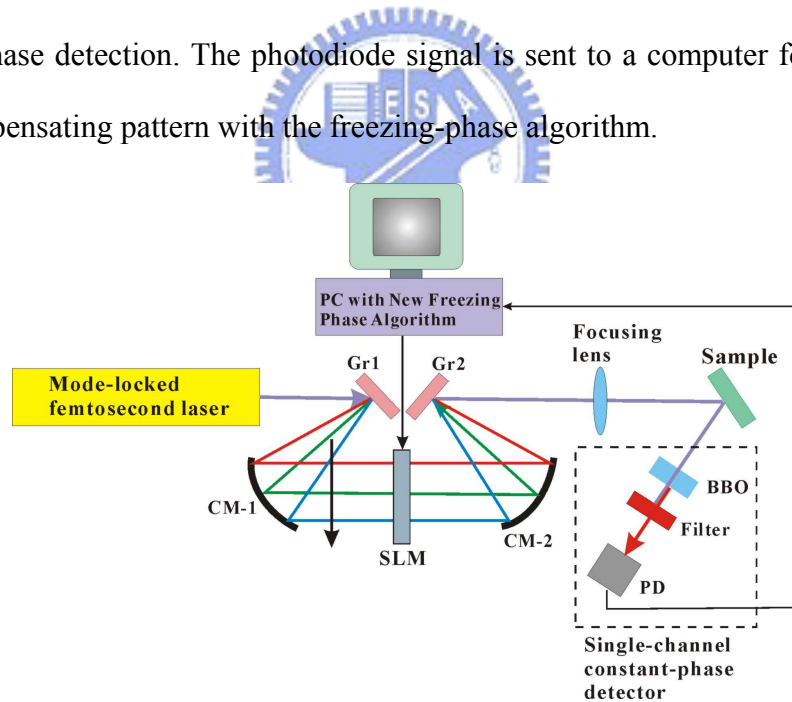


Fig. 3.2: Schematic of the adaptive coherent control system with an all reflective $4\text{-}f$ pulse shaper used in this study.

3.3 RESULTS

A. Simulation

To devise an efficient freezing phase scheme, we first conduct a series of model calculations. The coherent optical pulse input into a 4- f pulse shaper is assumed to have a Gaussian profile with pulse duration of 60 fs (FWHM) and a central wavelength of 1.252 μm . The coherent pulse is assumed to be phase distorted with a phase profile of $15[(i-64)/64]^2 + 7[(i-64)/64]^3 - 7[(i-40)/64]^4 - 8[(i-60)/64]^5$, where i denotes the position index of pixel.

Figure 3.3 describes the flow chart of our freezing-phase procedure. The simulation starts with grouping the SLM pixels into two classes: The first group plays the role of phase modulation. The other group is used as the reference. We vary the phase of the modulation group from 0 to 2π to generate SH modulation pattern. The spectral phase of the modulation group can be determined from the modulation pattern and is fixed to this value. The procedure is repeated by regrouping the SLM pixels until the phase retardations of all pixels are adjusted.

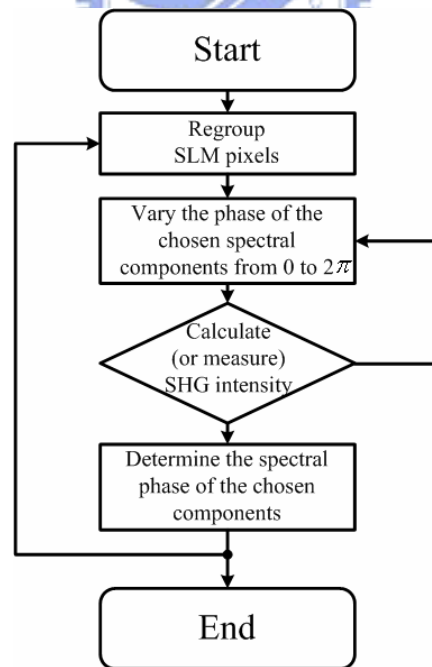


Fig. 3.3: Flow chart depicts the procedure used to implement the freezing-phase scheme into the theoretical and experimental studies

A.1 Freezing procedure with a left-to-right scan scheme

The intensity profile of the input pulse is shown in Fig. 3.4(b) with filled circles. In Fig. 3.4(c) the curve with open circles denotes the corresponding distorted spectral phase profile. A phase-freezing procedure with a left-to-right scan of SLM pixels is applied to compensate for the phase distortion. Fig. 3.4(a) depicts the time course of the maximum SH intensity during the phase-freezing procedure. Note that the SH signal is normalized to that with a transform-limited pulse (TLP). We found that significant SH signal change always occurs at those pixels locating within the spectral range (*i.e.*, 1.20 μm →1.29 μm) of the input pulse. SH intensity reaches 75% of the transform-limited value after first scan and 98% after second scan.

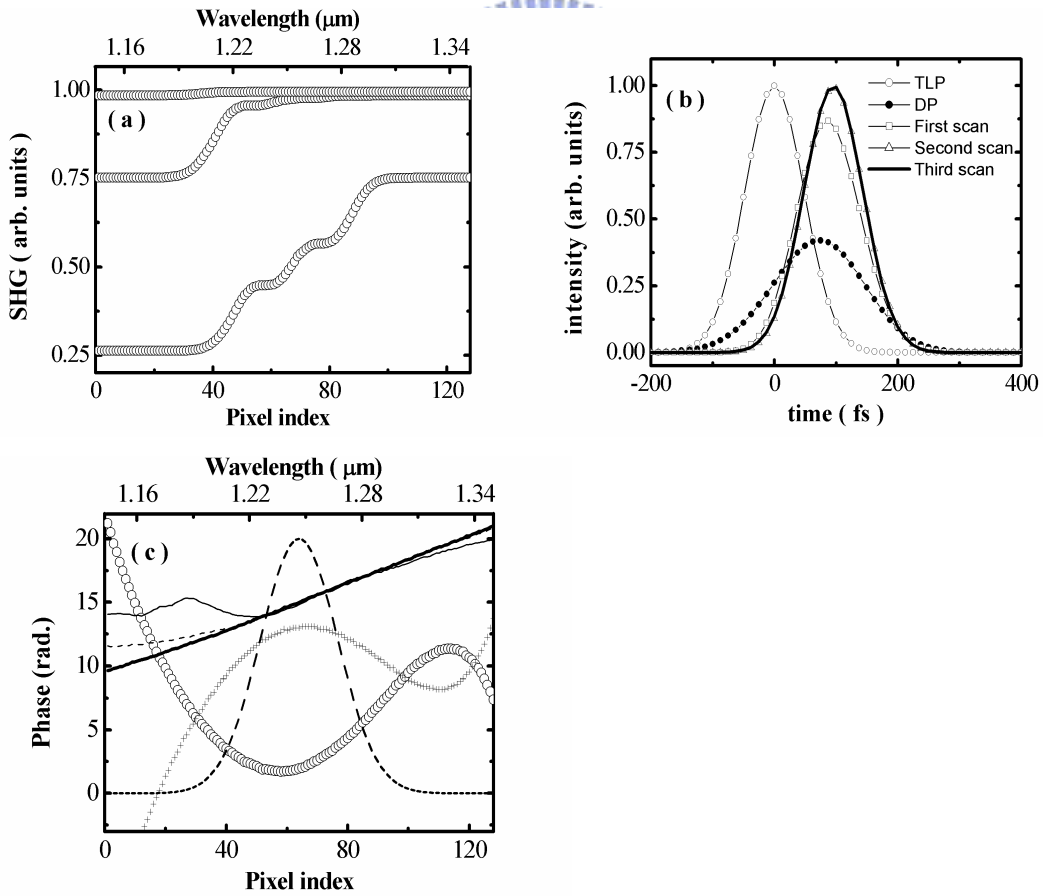


Fig. 3.4: (a) Time course of the maximum SH intensity during the phase-freezing procedure with a left-to-right scan scheme; (b) the intensity profiles of

transform-limited pulse (TLP), phase-distorted input pulse (DP), and phase-compensated pulse after first, second, and third freezing phase scans; (c) the spectral phase profile of the input pulse (open circles), compensating phase profile (crosses), and error phase profiles after first (thin solid curve), second (short dashed), and third (thick solid curve) freezing phase scans.

The corresponding pulse profiles after the first (open squares), second scan (open triangles) and third scan (thick solid curve) are presented in Fig. 3.4(b). The pulse spectrum (dashed curve), the distorted phase (DP, open circles), the compensating phase (CMP, cross symbols), and the error phase obtained with a summation of DP and CMP are shown in Fig. 3.4(c). After the first scan, the root-mean-squared (rms) deviation of the error phase from a linear-phase decreases to 1.995. It can be further reduced to 0.640 by the second scan and to 0.095 by the third scan. In the best result of phase compensation only linear error phase term was left. Note that linear phase term in the frequency domain only results in a temporal shift (see Fig. 3.3(b)) of the entire pulse. Thus with the time invariance principle, our phase retrieval process does not lose any information about pulse characteristics.

A.2 Freezing procedure with a center-to-two sides scan scheme

As shown in the previous section, SH signal was found to change significantly with phase retardances of those pixels locating within the spectral range of the input pulse. To use this finding efficiently, we design a new scan scheme which starts from the central pixel and proceeds helically toward both sides of SLM. Fig. 3.5 presents the simulation results. We found that this scan scheme is indeed more efficient than the first scheme. The SH intensity increases to 92% of the transform-limited value after the first scan and the rms deviation of the error phase decreases to 1.356. With

just two scans the rms deviation is reduced to as small as 0.374.

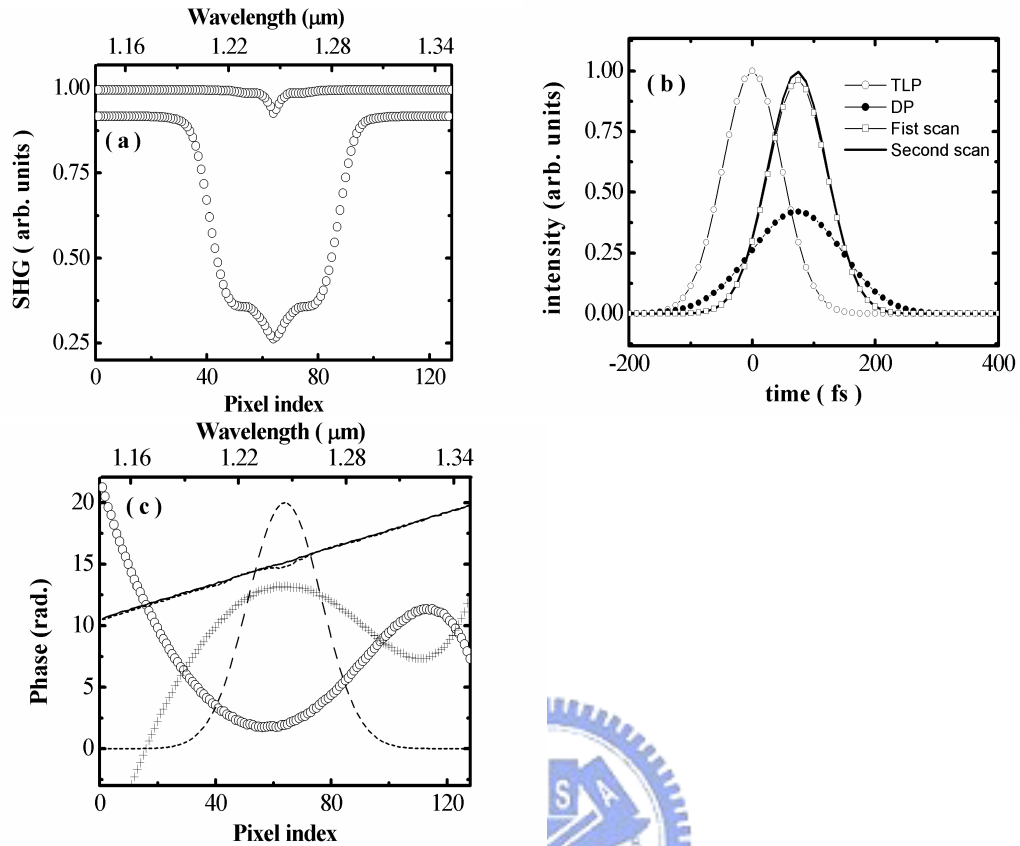


Fig.3.5: Time course of the maximum SH intensity during the freezing phase procedure with a center-to-two sides scan scheme; (b) the intensity profiles of transform-limited pulse (TLP), phase-distorted input pulse (DP), and phase-compensated pulse after first, second, and third freezing phase scans; (c) the spectral phase profile of the input pulse (open circles), compensating phase profile (crosses), and error phase profiles after first (thin solid curve), and second (short dashed) freezing phase scans.

A.3 Freezing procedure with a cascading thinning-out scheme

To devise an efficient procedure with higher noise immunity, we implement a special thinning-out scheme in our phase freezing process. We used a pixel-grouping method similar to that reported by Mizoguchi, *et al* [11]. The pixel numbers of the reference and the modulation groups vary from 64:64 (2s), 96:32 (4s), 112:16 (8s),

120:8 (16s), 124:4 (32s), 126:2 (64s), and 127:1 (128s) with ns denoting the number of pixel segments.

The freezing process starts with 2s thinning-out scheme and ends with 128s. Except the scheme 2s, which has only one configuration, there are n different arrangements for the scheme ns . The pixel segments cycle through SLM during each freezing stage. From the simulation result shown in Fig. 3.6(a), we found that the phase compensation almost completes at the stage 64s. The resulting pulse profiles and phase patterns after each phase compensation stage are presented in Fig. 3.6(b) and 3.6(c). Although the rms deviation of the error phase appears to be larger than that with the center-to-two sides scan scheme, this method is superior in noise immunity, which will be detailed in the next section.

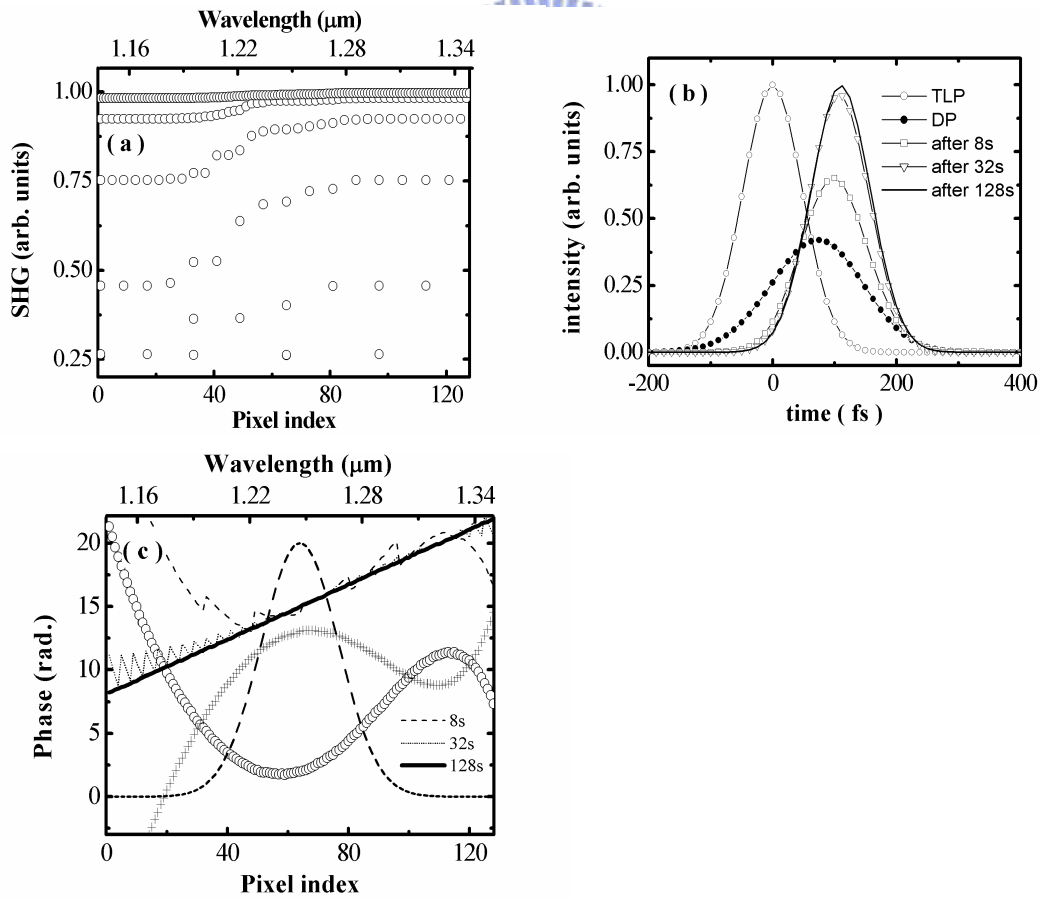


Fig. 3.6: Time course of the maximum SH intensity during the freezing phase procedure with a cascading thinning-out scheme; (b) the intensity profiles of

transform-limited pulse (TLP), phase-distorted input pulse (DP), and phase-compensated pulse after first, second, and third freezing phase scans; (c) the spectral phase profile of the input pulse (open circles), compensating phase profile (crosses), and error phase profiles after 8s (short dashed), 32s (dotted), and 128s (thick solid curve) freezing phase scans.

A.4 Noise influences on various freezing phase schemes

To properly assess the noise influences on the freezing phase schemes, we divide noise source into two terms: the first one is a multiplicative noise which could originate from the intensity fluctuation of coherent pulses. The second term is an additive noise which mainly comes from thermal noise in detection and feedback electronics. We assume each of the multiplicative noise and additive noise to be 5% of the maximum optical signal received.

By averaging ten phase compensation runs with each freezing scheme, we can obtain high-quality time course of maximum SH signal as a function of the number of freezing steps used. The results are shown in Fig. 3.7. It can be found that noise can degrade the quality of SH signal detection and therefore leads to an incorrect phase determination. We can combine N-neighboring pixels into one group to improve the accuracy of phase determination. Among the three above-mentioned methods, phase freezing with cascading thinning-out scheme appears to be the fastest method to reach the optimum solution. The slight decrease in SH intensity after 90 freezing steps is mainly caused by erroneous phase determination. This is supported by the observation that the signal level after the thinning-out scheme of 128s is close to the noise level (10%). Further phase freezing step beyond this point can not improve the result. Therefore in real application, we shall stop the freezing procedure in time based on the noise level encountered.

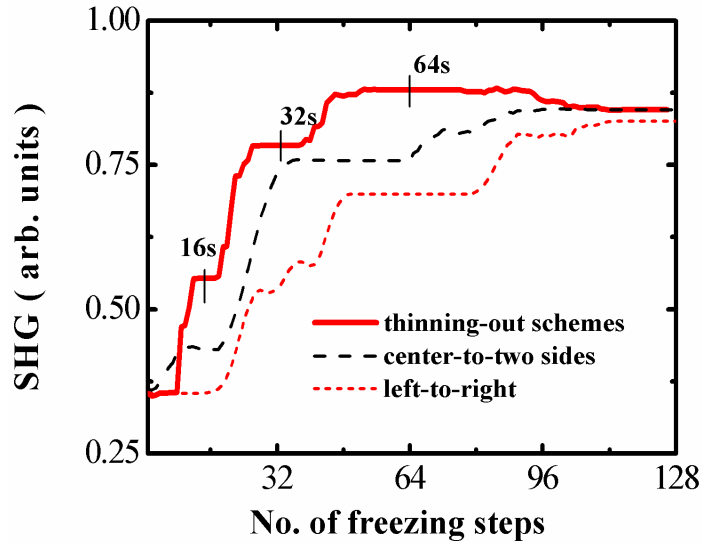


Fig. 3.7: Time courses of SH signal as a function of the number of freezing steps with a variety of freezing procedures: cascading thinning-out scheme (solid curve), a center-to-two sides scan scheme (long-dashed curve), and left-to-right scan scheme (short-dashed line).



B. Experimental Results and Discussion

B.1 Phase retrieving from phase-sensitive second-harmonic patterns

An experimental verification of the new freezing phase scheme starts with grouping of the SLM pixels into two classes: the first group, which is composed of three consecutive pixels, plays the role of phase modulation. The other group, which contains the rest pixels, is used as the reference. We vary the phase of the modulation group from 0 to 2π to maximize the SH intensity. The procedure repeats by regrouping the SLM pixels until the phase retardations of all pixels are adjusted.

Figure 3.8 shows the measured SHG intensity of the optical pulse reflected from a gold-coated mirror. The spectrum of the mode-locked laser pulse is also plotted to label the related spectral positions of the SLM pixels. The experimental results confirm that the SHG modulation is proportional to the amplitude of the chosen

spectral components as predicted by Eq. (6). The SH modulation pattern shifts, reflecting the spectral phase of the optical field. Once the chosen pixels lie outside the spectral range of the coherent pulse, the SH intensity modulation is no longer observable. These findings reveal the spectral phase profile of a coherent pulse to be deducible from the measured SH patterns by adjusting SLM retardation with a pulse shaping apparatus.

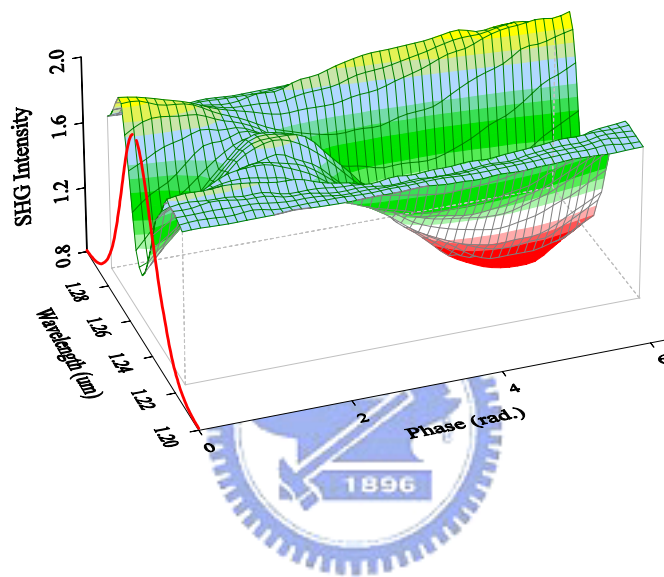


Fig. 3.8: Dependence of the measured SHG intensity of an optical pulse reflected from a gold-coated mirror on the phase retardance of three consecutive pixels of SLM.

B.2 Complete-field characterization of semiconductor saturable absorber mirrors with an adaptive control pulse shaper

InAs quantum dots (QDs) have important applications for ultrafast optical shaping at 1.3 μm . Under conditions of strong excitation, the absorption is saturated because possible initial states of the pump transition are depleted while the final states are partially occupied. Within 50–300 fs of excitation, the carriers in each band

thermalize, and this leads to a partial recovery of the absorption. The faster time constant is more effective in shaping subpicosecond pulses [20].

Saturable Bragg reflector (SBR) structure consists of a highly reflective Bragg mirror and quantum well or quantum dots embedded in it. By proper choice of the position of the saturable semiconductor layer it is possible to change the effective field that bleaches its optical absorption and therefore the saturation fluence of the device. This type of device is cheaper, more robust, and has quite a low insertion loss. The main limitation of SBR is most probably the strong wavelength dependence of the group delay introduced by the structure, which might be a problem for generating very short (<40 fs) pulses or for having large tuning range with fixed pulse parameters [21]. It is therefore important to characterize the complete-field profile of femtosecond optical pulse reflected from a variety of SBR structures in order to reveal the underlying pulse distortion processes. We employ our newly developed adaptive control apparatus on three types of SBR samples.

The first SBR device comprises of two $\text{Ga}_{0.47}\text{In}_{0.53}\text{As}$ quantum wells which are embedded in an $\text{Al}_{0.48}\text{In}_{0.52}\text{As}$ quarter wave layer on a distributed Bragg reflector (DBR) stack (hereafter is abbreviated as *d*-QW). The DBR stack is formed with 25 pairs GaAs/AlAs designed to yield a Bragg wavelength at $\lambda_B=1.23 \mu\text{m}$. The other is self-assembled InAs quantum-dots layer embedded in a quarter-wave-thick (QD- $\lambda/4$) or half-wave-thick (QD- $\lambda/2$) GaAs layer on a DBR stack. The DBR of the two devices is identical and contains 21-periods stack of 97 nm/112 nm GaAs/ $\text{Al}_{0.92}\text{Ga}_{0.08}\text{As}$. The DBR was designed to yield high reflection at 1.3 μm . The schematic device structures with the corresponding field distribution at a wavelength of 1.25 μm are depicted in figure 3.9.

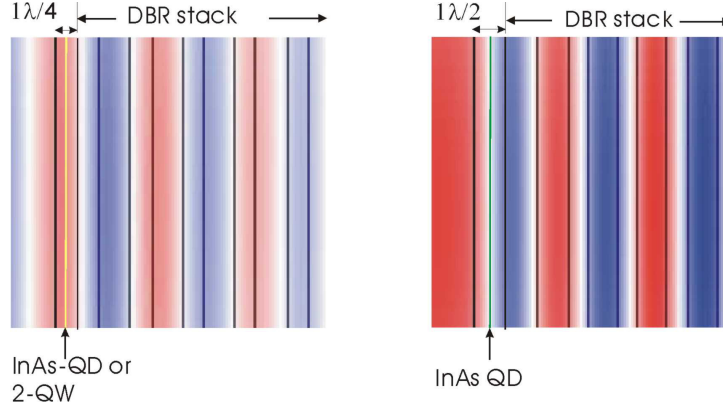


Fig. 3.9: Calculated field distribution (with blue-red color coding) is presented with the device structure of saturable absorber Bragg reflectors with InAs-QD or *d*-QW embedded in a (a) $\lambda/4$ -thick layer or (b) $\lambda/2$ -thick layer.

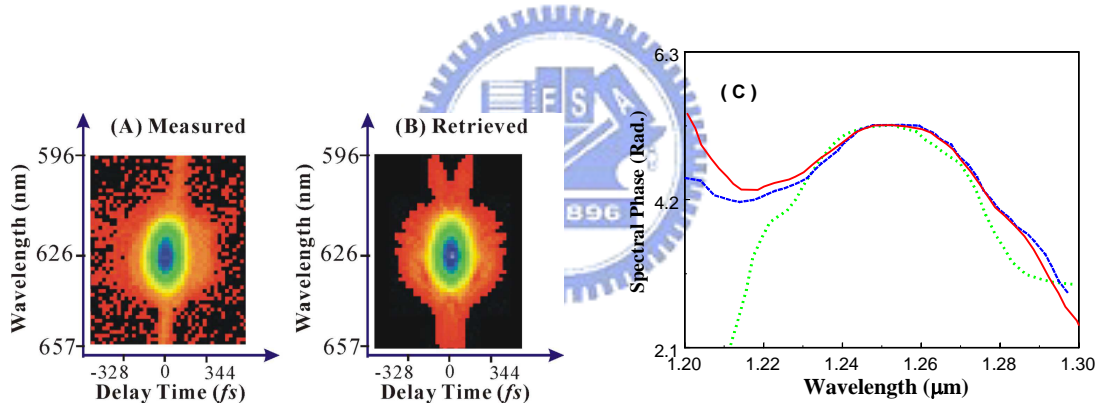


Fig. 3.10: (a) Measured and (b) retrieved SHG-FROG patterns of femtosecond optical field at $1.25 \mu\text{m}$ reflected from the QD- $\lambda/2$ SBR and (c) the retrieved spectral phase profiles from *d*-QW (solid curve), QD- $\lambda/4$ (long dashed) and QD- $\lambda/2$ (short dashed line) SHG-FROG traces.

We first employ SHG frequency-resolved optical gating (SHG-FROG) technique [21] to characterize the complete-field profiles of the femtosecond pulses reflected from the three SBR devices. The result for the QD- $\lambda/2$ structures is shown in Fig. 3.10. The experimental SHG-FROG trace was retrieved with an error of 0.0025. The

retrieved spectral phase profiles for the three SBR devices are presented in Fig. 3.10 (c) and are found to overlap with each other near the central region but significant difference can be observed at the tails of the spectra of QD- $\lambda/4$ and QD- $\lambda/2$. As shown in Fig. 3.9 the field strength experienced by the InAs QDs in QD- $\lambda/2$ is smaller and therefore we expect to observe weaker pulse shaping effect and therefore larger phase distortion in QD- $\lambda/2$.

After performing the pulse analysis with standard SHG-FROG, we then proceed to diagnose the complete-field characteristics with our freezing phase adaptive phase compensation apparatus. The results are summarized in Fig. 3.11. We first use the modulation depth of SH signal (see Fig. 3.8) to determine the spectral profile. Fig. 3.11(a) presents a direct comparison of the deduced spectral profile of optical pulse reflected from the d -QW sample from freezing-phase algorithm (FA) and that measured with Fourier-transformed infrared spectroscopy (FTIR). An excellent agreement was found, indicating that our adaptive phase compensation scheme not only be able to yield the spectral phase profile but also the amplitude of a coherent optical pulse. We then present the measured spectral phase profiles with FA for the three SBR devices in Fig. 3.11(b). The global features of the measured spectral phase profiles are similar to that obtained with SHG-FROG technique. The most deviations occur at the regions with small spectral amplitude where retrieving with FROG algorithm is usually less reliable. The slight shift of the QD- $\lambda/2$ spectral phase profile (short dashed curve) from d -QW (solid curve) and QD- $\lambda/4$ (long dashed) also occurs in the spectra measured with FTIR. Note that the device structure of QD- $\lambda/2$ is very similar to QD- $\lambda/4$ except a twice thicker QDs embedded layer employed in QD- $\lambda/2$. The clearly distinguishable differences in the spectral phase profiles ensure that our new complete-field characterization scheme is sensitive and accurate to reveal influence on femtosecond optical pulse with subtle change in SBR structures.

Furthermore, unlike SHG-FROG with pulse characteristics to be retrieved with sophisticated mathematical procedure, our method belongs to a direct measurement approach.

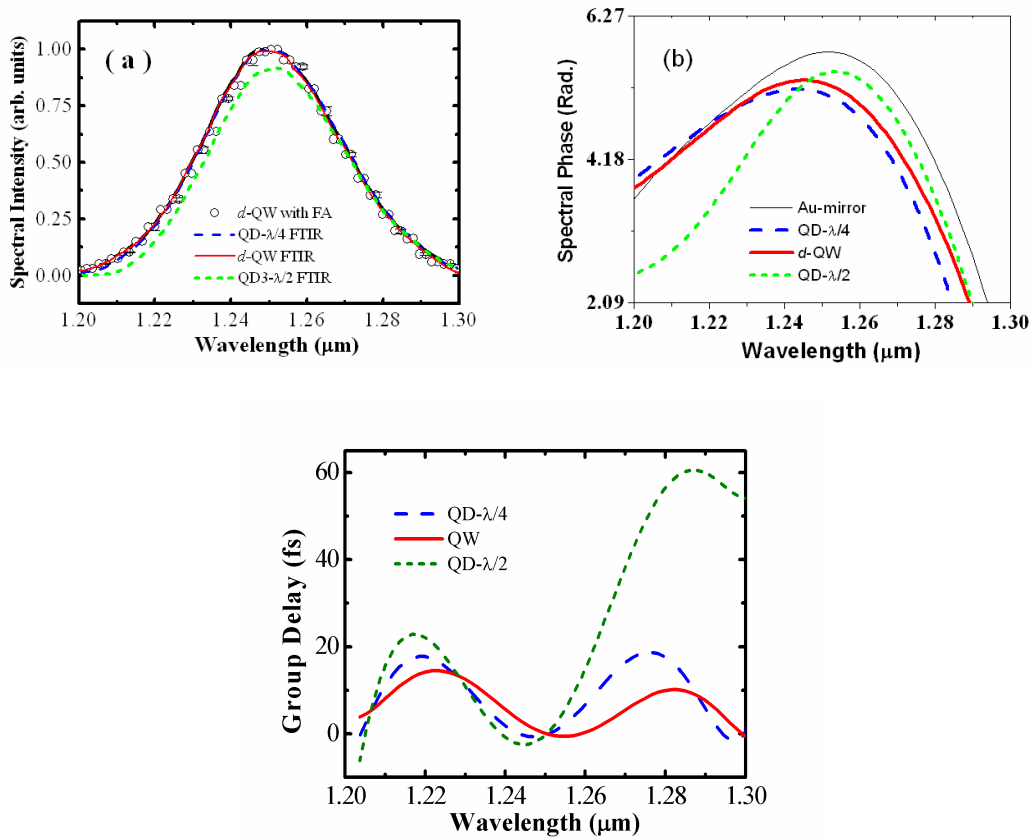


Fig. 3.11: (a) Spectral profiles of optical pulses reflected from d -QW (open circles) measured with freezing-phase algorithm (FA) and from d -QW (solid curve), QD- $\lambda/4$ (long dashed), QD- $\lambda/2$ (short dashed) with Fourier-transformed infrared spectroscopy (FTIR) (b) Spectral phase profiles from Au-mirror (thin solid curve), d -QW (thick solid curve), InAs QD- $\lambda/4$ (long dashed), and InAs QD- $\lambda/2$ (short dashed) deduced with phase freezing scheme; (c) group delay time of the three SBR devices over the entire pulse spectral range.

As explained in the previous paragraph, the main limitation of SBR in ultrashort laser application is the strong wavelength dependence of the group delay introduced by device structure. With the measured spectral phase profiles we can further deduce the group delay caused by the SBR devices. To properly remove influences from laser optics, the phase profile of an optical pulse reflected from a gold mirror placed at the same position of the SBR devices were also measured. The group delay times of the SBR devices were deduced by first taking a difference between the spectral phase profiles of SBR and Au mirror. We then differentiated the phase difference profiles with angular frequency to yield the group delay times. The results are presented in Fig. 3.11 (c), show that the *d*-QW SBR exhibits much weaker wavelength-dependent group delay within the entire spectral range of the optical pulse. Indeed this device had been designed for passively mode locking femtosecond laser at 1.25 μm and was confirmed experimentally to be able to generate femtosecond laser pulse with pulse duration less than 60 *fs*. As expected, among the three SBR structures the QD- $\lambda/2$ shows largest variation in group delay within the spectral range, especially for the spectral components with wavelength longer than 1.27 μm . The larger variation in group-delay by QD- $\lambda/2$ can originate from weaker field strength being experienced by the InAs QDs and therefore weaker pulse shaping effect is yielded.

The position of the saturable absorber layer inside the structure is an important design parameter. Usually it prefers to place the saturable absorber layer at a high field location, such that the effective saturation fluence of the device is reduced. However, Keller, *et al.* had recently pointed out that this may cause a pronounced absorption dip at the resonance wavelength, and the extra loss would push the lasing wavelength away from the negative GVD regime [21]. Therefore, those researchers suggested the absorber layer to be positioned close to the field minimum.

B.3 Comparison to genetic algorithm

For adaptive coherent control applications, time to achieve optimum control is the major concern. In Fig. 3.12, we present a comparison of the measured SHG intensities with the freezing phase scheme and that with a genetic algorithm [14-16]. To ensure the comparison being taken on a similar base, the genetic algorithm is implemented with a 3s thinning-out scheme [11]. It was shown that the total number of SLM adjustments with our freezing phase algorithm can be as low as 700 to yield a phase resolution of 2° . Therefore, adaptive coherent optimization with our new scheme can be greatly shortened. Furthermore, the quality of the optimization with our freezing algorithm is also slightly better than that with GA. For a practical application, noise influences on the SH signal detection shall be taken into account. In this regard, GA was found to be more sensitive to the fluctuation of laser power. When the laser power decreases, GA tends to judge all individuals after this power reduction to be poorer than that of the previous generation. This erroneous judgment does not happen with the freezing phase algorithm (FA).

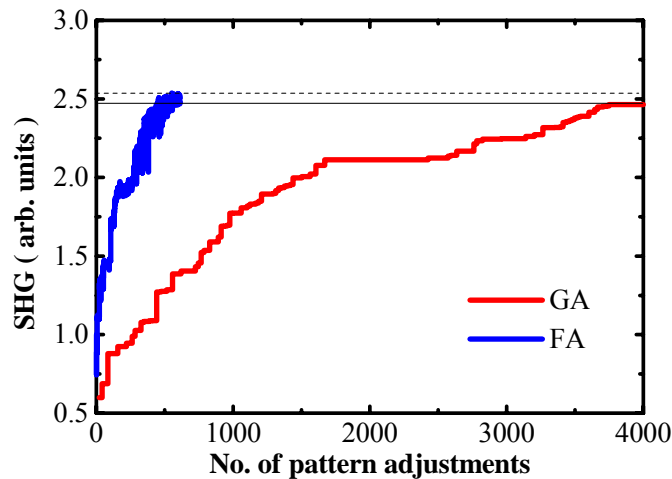
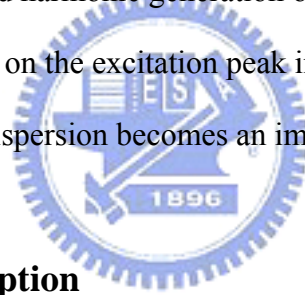


Fig. 3.12: Measured SHG is plotted as a function of the number of phase adjustments with the freezing phase algorithm (FA: blue solid curve) and genetic algorithm (GA: red-colored).



Chapter 4 Coherent Control Nonlinear Optical Microscopy

Technique just beginning to be explored is the characterization of ultrashort pulses at the focus of high numerical aperture objective used for multiphoton microscopy [26, 27, 28]. Precise characterization of the focused pulses is required to produce optimal nonlinear optical image with multiphoton microscopy because the image quality critically depends on the size of the focal spot and the pulse profile. Microscope objective used to produce the tightest focus, and hence the best spatial resolution, however, encounters difficulties with ultrashort laser pulses with broad spectral bandwidth. For second harmonic generation or multiphoton microscopy, the NLO signal critically depends on the excitation peak intensity used. How to compensate for group delay dispersion becomes an important issue.



4.1 Experimental Description

Fig. 4.1 shows the experimental layout for our multiphoton microscopy. The pulse passes through the pulse shaper and is tightly focused by a $50\times/0.55$ NA microscope objective lens. Intensities at the focal point can easily reach 10^{13} W/cm². The objective lens focuses the laser light to a diffraction-limited spot. The sample is mounted on a commercial XY scanning stage. The emission light was collected by the same objective lens and is sent into a spectrometer equipped with a cooled PMT tube. We use SHG signal (2ω) or fluorescence signal ($1\omega'$) as the feedback signal for adaptively coherent control. A PC with an implementation of freezing phase algorithm controls the pulse shaper to optimize the signal detected.

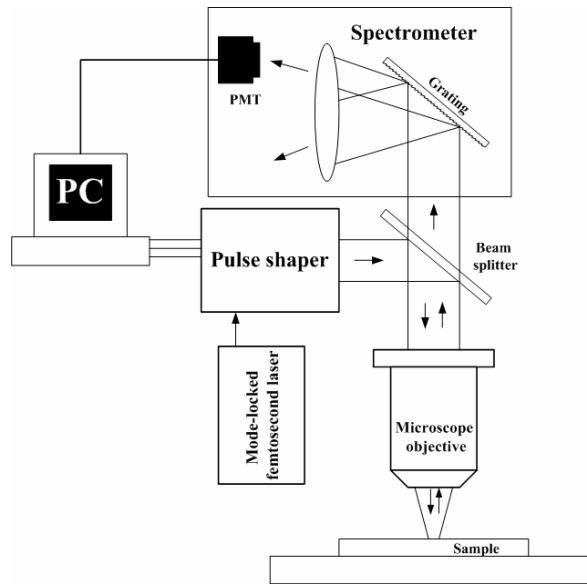


Fig. 4.1: Schematic arrangement for multiphoton microscopy. The pulse goes through the pulse shaper and tight focused by a $50\times/0.55$ NA objective. Intensities at the focal point can easily reach 10^{13} W/cm²

The sample used is the QD- $\lambda/2$ -sample described in Chapter 3, which is an InAs self-assemble quantum-dot layer embedded in a half wave layer of GaAs on a DBR structure. InAs quantum dots have important applications for ultrafast optical switching at $1.3 \mu\text{m}$. The semiconductor saturable absorber with 21-periods $97 \text{ nm}/112 \text{ nm GaAs}/\text{Al}_{0.92}\text{Ga}_{0.08}\text{As}$ is depicted in the inset of Fig. 4.2. The energy-level diagram of the sample is also shown in Fig. 4.2.

An ultrashort optical pulse can excite valence electrons from the highest valence band to conduction band. The optical excitation could return to the ground state via the following two processes: The optical excitation can directly return to the ground state within coherent time and emits SH photon 2ω . The second way is that the optical excitation undergoes dephasing and then energy relaxation to the lowest unoccupied band and emits fluorescent photon at ω' . Note that both SHG and two-photon excited fluorescence (TPF) can originate from the same two-photon-excited level. The issue becomes how much population on this level after two-photon excitation.

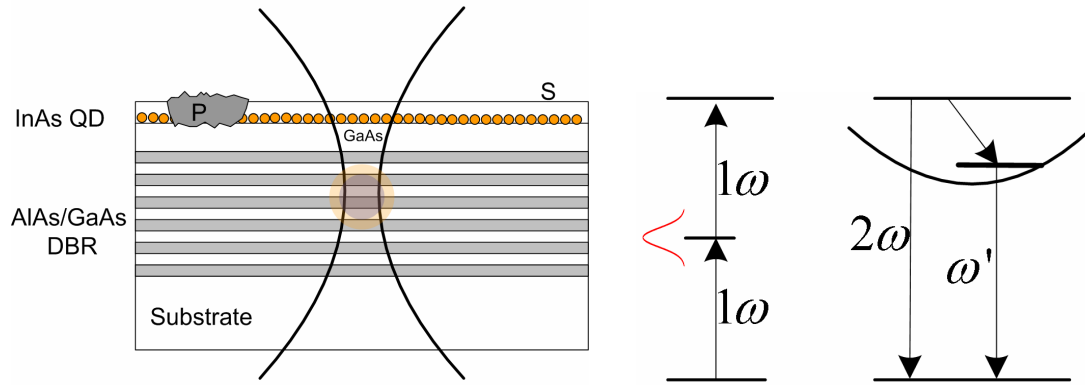


Fig. 4.2: Right: InAs self-assembled quantum-dot layer embedded in a half wave layer of GaAs on a DBR structure. The DBR stack is formed with 25 pairs GaAs/AlAs designed to yield a Bragg wavelength at $\lambda_B=1.23 \mu\text{m}$. The focal point of the NLO microscope objective lens is positioned to under the surface of the sample. Therefore optical pulses must penetrate a distance about $50 \mu\text{m}$, before reach the focal point. The area labeled by ‘P’ displays some epi-defects on the surface. Other normal area is labeled by ‘S’.

Left : Energy-level diagram of a resonant TPA in semiconductor saturable absorber. The pulse spectrum is centered on the two-photo transition frequency (1ω) at 1250 nm, with the bandwidth of 39 nm (FWHM). The frequency of SHG (2ω) corresponds to 625 nm. The frequency of the $1\omega'$ resonant transition corresponds to 868 nm.

4.2 SHG as the Adaptive Coherent Control Signal

In this study, we first chose SHG as our adaptive coherent control signal. The absorption of exciting photons by InAs quantum dots can be observed in an spectral sensitivity curve. We shall discuss its influence on the spectral phase profile.

SHG efficiency is known to be sensitive to the phase of optical field. There are three plausible phase distortion sources to be met by ultrashort excitation pulse before it reaches the NLO signal generation region. The first source is the intrinsic phase distortion of the laser, whose pulse compression prism pair in the laser oscillator is not properly adjusted to completely compensate the group velocity dispersion of each spectral component. This leads to non-transform-limited pulses from the laser oscillator with frequency chirping. The second source could originate from the

microscope objective lens as the ultrashort pulse passes through the objective lens. Each spectral components of the pulse may arrive at the focal point with different delay time. For a femtosecond ultra short pulse, the pulse can be broadened significantly as it goes through a dispersive material. The last source comes from sample itself. The NLO signal generation regime may bury under the sample surface with a certain distance. Such a thin surface layer affects the incident ultrashort pulse.

A personal computer equipped with the freezing phase algorithm deduces the phase retardation pattern for compensating the overall spectral phase distortion from those three phase distortion sources. In Fig. 4.3(b) shows a comparison of two-photon excited fluorescent images taken from the same area of QD- $\lambda/2$ semiconductor saturable absorber mirror. The first image is measured with ultrashort pulses by taking SLM pixels to be all-zero phase retardation. The second image is taken with an optimum coherent control phase pattern used for compensating the phase distortions from laser optics, objective lens, and the surface layer of the sample. The optimum coherent control phase pattern (the green-colored curve in Fig. 4.3(a)) was obtained by optimizing the SHG signal generated. It is shown that three-time better contrast for two-photon excited fluorescent image can be achieved with the coherent control phase profile.

A small dip centered at a wavelength of 1.253 μm in the spectral sensitivity plot of SHG (green dash line) can be seen. Here the spectral sensitivity of SHG is defined as the difference between the maximum and minimum SHG signals when we adjust a specific spectral component of the ultrashort excitation laser pulse via SLM128. This observed wavelength with SHG sensitivity dip is equal to one of the PL peaks of the self-assembled InAs QD layer. Before the pulses arrive at the SHG generating region, some excitation photons at 1.253 μm are absorbed by the InAs QD layer. This causes a gap at 1.253 μm in the SHG spectral sensitivity curve.

Silberberg's group reported that transform-limited pulses are not optimal for generating resonant multiphoton transitions [29]. An intermediate single-photon-resonant level substantially varies the incoming phase profile of the excitation pulses. The sample they used is rubidium atomic vapor which is spatially uniform. In our case, only a few percent of the incoming electric field is altered by the thin self-assembled InAs quantum-dots layer. The intermediate level is easily saturated. When incoming photons at 1.253 μm bleach the optical absorption, this intermediate level becomes ineffective for the rest optical excitation.

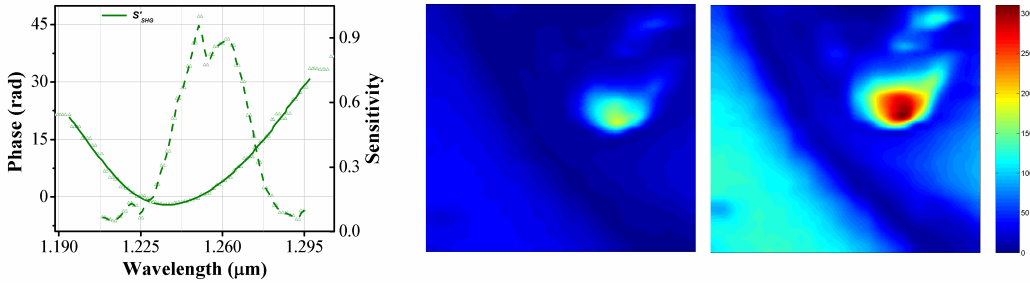


Fig. 4.3: **Left:** The phase profile (green solid line) and spectral sensitivity plot of SHG (green dashed line) obtained by freezing phase algorithm. **Right:** Two images with 40 $\mu\text{m} \times 30 \mu\text{m}$ taken from the same area of QD- $\lambda/2$ semiconductor saturable absorber mirror. The first image is measured with ultrashort pulses by taking all SLM-128 pixels to have zero phase retardation, and the second image is taken with a optimum coherent control phase pattern used for compensating the phase distortions from laser optics, objective lens, and the surface layer of the sample. Three times better contrast for two-photon excited fluorescent image was achieved.

If a two-photon-transition is not affected by an intermediate level [30], the signal amplitude of the two-photon transition can be simply expressed by

$$E_{SHG}(2\omega) \propto \int E(\omega + \Delta)E(\omega - \Delta)d\Delta.$$

This equation indicates that two-photon transition could be generated from all pair of photons with frequencies that can sum up to yield the final transition frequency $(\omega - \Delta) + (\omega + \Delta) = 2\omega$. The two-photon absorption (TPA) rate can therefore be maximized by a transform-limited pulse, where all the spectral elements of $E(\omega)$ have the same

phase and TPA transition amplitude be summed up constructively. For third harmonic generation (THG) without a resonant intermediate level, the THG signal amplitude can be expressed as

$$E_{THG}(3\omega) \propto \int E_{SHG}(2\omega + \Delta)E(\omega - \Delta)d\Delta.$$

It can also be maximized by transform-limited pulse.

We combine the SHG and THG equations with an ultrashort pulse, which is modulated by two periodic phase patterns shown in Fig. 4.4. The measured results on the QD- $\lambda/2$ InAs SBR with those two periodic phase modulation patterns are plotted on the left column of Fig. 4-4. By doing this, we confirm that the influence of an intermediate level on SHG, TPA or THG to be negligible. The input pulses with different phase profile do not vary the shape of fluorescence. The energy relaxation process to the 868-nm level doesn't have a direct relation with the input pulse. The fluorescent efficiency is only determined by how many electrons populate the 868 nm level.

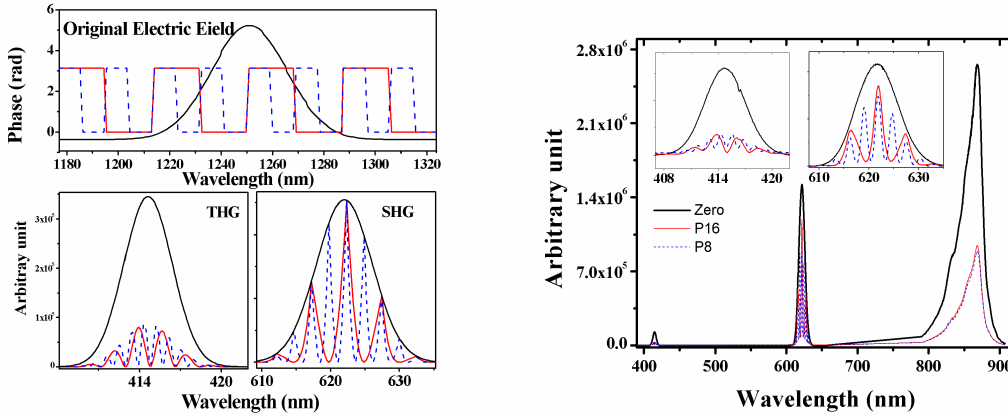


Fig. 4.4: **Left :** Some simulated results of SHG and THG without an intermediate resonant energy level. The material is assumed to be excited by an ultrashort pulse with two different periodic phase modulation patterns. **Right :** Measured results of the QD- $\lambda/2$ InAs SBR with those two periodic phase modulation patterns.

We conclude that the final phase retardation pattern obtained by freezing phase algorithm could compensate the time delay between all spectral components of pulses

and the spectral sensitivity can exhibit the minor absorption of photons by material.

4.3 Two-Photon-Excited Fluorescence as the Adaptive Coherent Control Signal

Because the efficiency of the two-photon excited fluorescence is sensitive to the phase profile of input pulse, in this section we shall use two-photon excited fluorescent signal as our coherent control signal. The decay time of the fluorescent signal is shorter than the pulse repetition period (10 ns) of the laser. Therefore the optical excitation is not accumulated.

On the QD- $\lambda/2$ InAs SBR sample, we select two different positions, which are labeled by P and S in the Fig. 4.5, for further investigation. The P-position looks like an epi-defect site that yields higher fluorescent signal compared to the surrounding area. The S-position exhibits a lower fluorescent signal than that from P-site. We can select the two-photon excited fluorescent signal from P site or S site as our coherent control signal. Similar to the SHG studied, two-photon excited fluorescence spectral sensitivity is defined to be the difference between the maximum and minimum two-photon excited fluorescent signals when we adjust a specific spectral component of the ultrashort excitation laser pulse via SLM128.

The red-colored dashed and solid lines in Fig. 4.5 present the spectral sensitivity and phase retardation profile [labeled by S'] for yielding maximum two-photon-excited fluorescence at S position. The resulting fluorescent spectrum peaks at 868-nm. The blue-colored dash and solid curves represent the spectral sensitivity and the phase retardation profile [P'] for generating maximum fluorescent signal at 886-nm at P position. The coherent control enhancement can be confirmed by using the S' phase profile, the 868-nm fluorescent spectrum is found to be higher than that used P' phase profile. Similarly, we also find that the 886-nm spectrum is

higher by using the P' phase profile (see the figure on the right-hand side of Fig. 4.5). Apparently, optical pulses with the phase pattern [P'/S'] is more suited for two-photon-excited fluorescence at the position of [P'/S'].

If we compare the two phase patterns that maximize SHG and TPF, we can find they are almost identical (see the green and red solid curves). This result indicates that ultrashort optical pulse with the phase profile can excite QD- $\lambda/2$ SBR at S position into the higher-energy level. The population of the two-photon excitation level becomes the common source of SHG and TPF. They differ only on the emission process of output photon. For SHG, the emission of output photon is a coherent process, while for TPF the emission is incoherent. The difference between SHG and TPF is very similar to the case of resonant Raman scattering and hot luminescence.

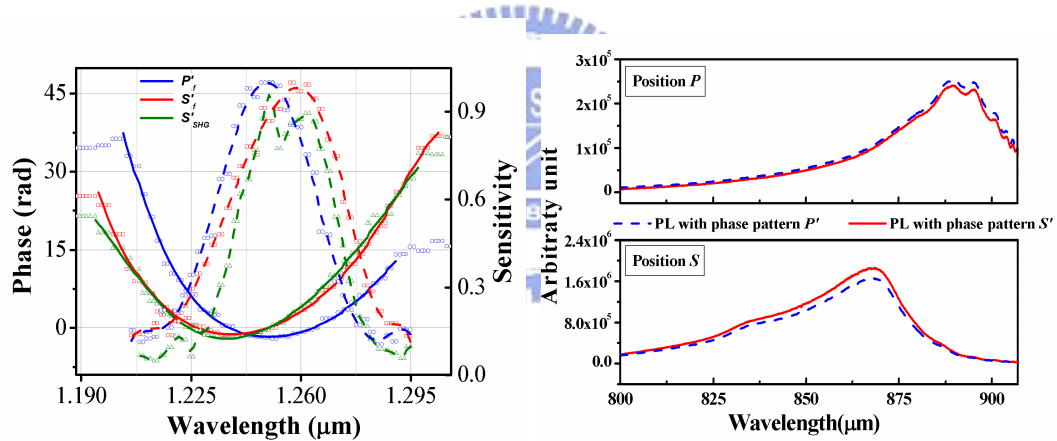


Fig. 4.5: Left: Two-photon-excited fluorescent (TPF) spectral sensitivity (dash line) and phase retardation pattern (solid line) used to yield maximum TPF signal from position P (blue) and S (red). Right: The phase patterns [P'] and [S'] can generate higher TPF from position P and S, respectively.

A. Explanation of the measured coherent control phase profiles

Here we offer two possible explanations for the difference of the coherent control phase profiles observed at two different positions P' and S':

- **Surface defects distort the phase profile of electric field:** If there are some impurities or defect on the sample surface, those impurities may

distort the phase of input ultrashort pulse before the pulse reaches the TPF generating point in the sample. The phase-only pulse shaper used in this thesis can adjust all spectral components of the pulse to allow them arrive at the TPF generating point simultaneously. The different TPF spectral sensitivity observed at P and S may due to that some spectral components of the input pulse are reflected differently by the sample surface. Since these spectral components do not arrive the TPF generating point, they can not contribute to the TPF.

- **The energy-level structure in defect area changes or shifts:** Impurities or defects can alter the electronic structure of semiconductor. This may cause the coherent control phase profile for TPF at *P* different from that from *S*. Some impurities may also introduce an intermediate level which is in resonance to the incoming photons.

Between the two possible explanations, the first one appears to be more likely than the other. We had carefully examined the spectrum of SHG and found that there is no sign of an intermediate resonant level involved in SHG. We therefore conclude that the epi-defect at P simply shifts the TPF frequency from 868 nm to 886 nm. No intermediate level which is resonant to incoming photons at 1.25 μm is identified. The InAs QD layer simply generates saturable absorption effect but does not contributes to resonant SHG, presumably owing its much smaller layer thickness than other DBR layers.

4.4 Coherent Control Tomography

Based on the former discussion, the TPF is sensitive to the surface condition of sample. The coherent control phase pattern needed to compensate for group delay dispersion of the surface layer differs with positions. We can therefore obtain

information about the surface profile by subtracting two TPF images with two different coherent control phase patterns. The results are shown in Fig. 4.6. The TPF images were formed by collecting the TPF signal while moving the sample with respect to the laser beam in a step-scan fashion. The top-left image indicates the result of a TPF scan at 868 nm under excitation of ultrashort optical pulses with phase profile P' . The top-right image is the same scan under excitation of ultrashort optical pulses with phase profile S' . The coherent control difference image resulting from subtracting those two TPF distributions exhibits some subtle variation within the bright spot. The intensity variation shall reflect the optical path variation of the surface layer. Surface properties of those areas are similar that the higher fluorescent efficiency is got with the same phase pattern.

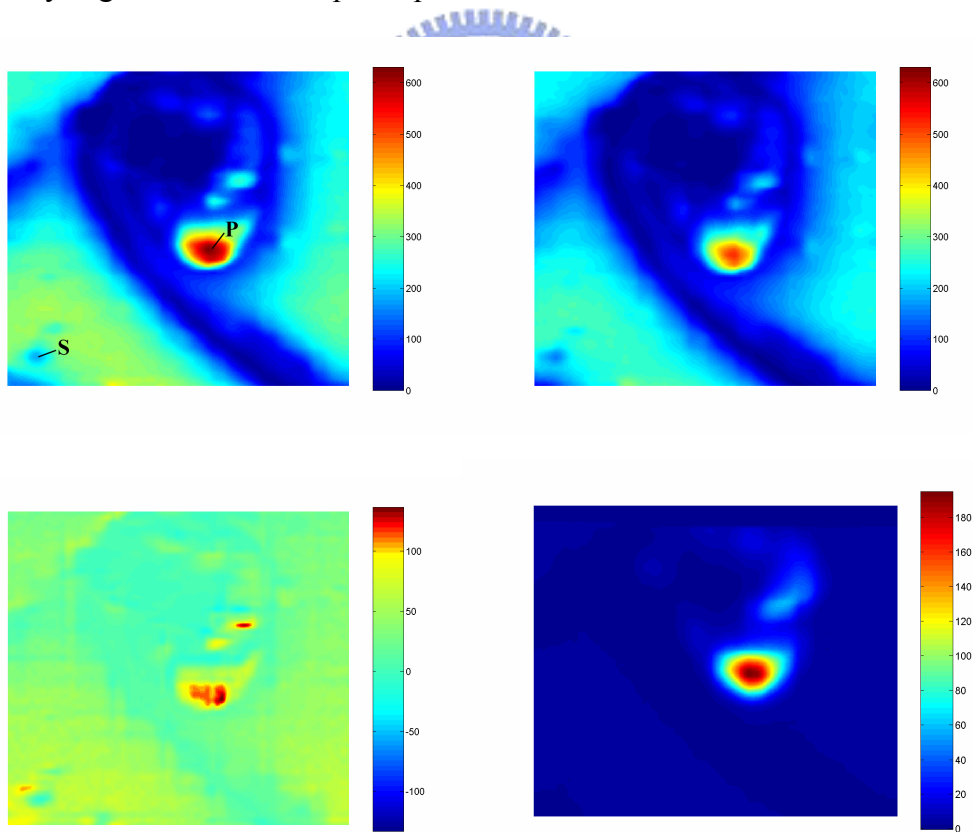


Fig. 4.6: Two TPF scans on a $70 \times 60 \mu\text{m}$ region of the semiconductor saturable absorber mirror. **Top left:** TPF image at 868 nm taken with coherent control phase pattern [P']. **Top right:** TPF image at 868 nm taken with coherent control phase pattern [S']. **Bottom left:** coherent control TPF difference map resulted from

subtracting those two TPF intensity distributions. **Bottom right:** TPF image at 886-nm with coherent control phase pattern [P'].



Chapter 5 Conclusion and Future Prospect

In this thesis, we demonstrate the optical synthesis technique for a desired ultrashort optical pulse with Gerchberg-Saxton algorithm (GSA). By using an initial random phase pattern, GSA achieves the target pulse faster as compared to that using an initial constant phase pattern.

Based on the result, we further developed a new freezing phase algorithm for complete-field characterization of femtosecond ultrashort pulse with a phase-only pulse shaping apparatus. The operational principle is based on the fact that the highest peak intensity corresponds to a complete frozen-phase state of all spectral components. Our experimental and theoretical results reveal several unique features and advantages. This freezing phase scheme had been employed for analyzing three types of semiconductor saturable absorber Bragg reflectors (SBR) and the detailed influence on phase distortion from subtle change in device structure can be revealed clearly. Our results show the scheme to be faster and more accurate for characterization and adaptive control of coherent pulses.

We applied this adaptive coherent control apparatus on nonlinear optical microscopy. The phase pattern needed to compensate for group delay dispersion from laser optics, microscope objective lens, and sample surface was retrieved and coherent control nonlinear optical images were obtained. From the coherent control spectral sensitivity of nonlinear optical signal generation we demonstrate that the effect of saturable absorption from ultrathin layer of self-assembling InAs QD can be revealed.

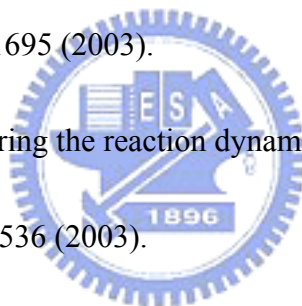
We believe that this technique shall be useful for various future applications

which require ultrashort pulse conversion, complete-field characterization and adaptive coherent control on the same setup.

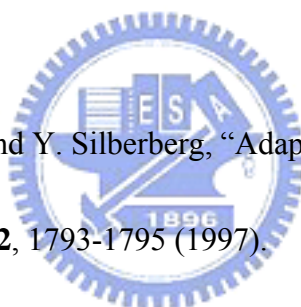


References

1. R. S. Judson and H. Rabitz, *Phys. Rev. Lett.* **68**, 1500 (1992).
2. N. Dudovich, B. Orion, and Y. Silberberg, *Nature* **418**, 512-515 (2002).
3. T. Brixner, N. H. Damrauer, P. Niklaus, and G. Gerber, "Photoselective adaptive femtosecond quantum control in the liquid phase," *Nature* **414**, 57-60 (2001).
4. Igor Pastirk, Johanna M. Dela Cruz, Katherine A. Walowicz, Vadim V. Lozovoy, and Marcos Dantus, "Selective two-photon microscopy with shaped femtosecond pulses," *Opt. Express* **11**, 1695 (2003).
5. C. Daniel, *et al.*, "Deciphering the reaction dynamics underlying optical control laser fields," *Science* **299**, 536 (2003).
6. A. Assion, T. Baumert, M. Bergt, T. Brixner, B. Kiefer, V. Seyfried, M. Strehle, and G. Gerber, "Control of chemical reactions by feedback-optimized phase-shaped femtosecond laser pulses," *Science* **282**, 919 (1998).
7. W. S. Warren, H. Rabitz, and M. Dahleh, *Science* **259**, 1581 (1993).
8. T. C. Weinacht, J. L. White, and P. H. Bucksbaum, "Toward strong field mode-selective chemistry," *J. Phys. Chem. A* **103**, 10166-10168 (1999).



9. R. J. Levis, G. M. Menkir, and H. Rabitz, "Selective bond dissociation and rearrangement with optimally tailored strong-field laser pulses," *Science* **292**, 709 (2001).
10. C. J. Bardeen, V. V. Yakovlev, K. R. Wilson, S. D. Carpenter, P. M. Weber, and W. S. Warren, "Feedback quantum control of molecular electronic population transfer," *Chem. Phys. Lett.* **280**, 151-158 (1997).
11. R. Mizoguchi, K. Onda, S. S. Kano, and A. Wada, "Thinning out in optimized pulse shaping method using genetic algorithm," *Rev. Sci. Instrum.* **74**, 2670-2674 (2003).
12. D. Yelin, D. Meshulach, and Y. Silberberg, "Adaptive femtosecond pulse compression," *Opt. Lett.* **22**, 1793-1795 (1997).
13. D. Meshulach, D. Yelin, and Y. Silberberg, "Adaptive real-time femtosecond pulse shaping," *J. Opt. Soc. Am. B* **15**, 1615-1619 (1998).
14. T. Baumert, T. Brixner, V. Seyfried, M. Strehle, G. Gerber, "Femtosecond pulse shaping by an evolutionary algorithm," *Appl. Phys. B-Lasers and Optics* **65**, 779-782 (1997).
15. E. Zeek, R. Bartels, M. M. Murnane, H. C. Kapteyn, and S. Backus, "Adaptive pulse compression for transform-limited 15-fs high-energy pulse generation," *Opt. Lett.* **25**, 587-589 (2000).



16. A. Efimov, M. D. Moores, N. M. Beach, J. L. Krause, and D. H. Reitze,
“ Adaptive control of pulse phase in a chirped-pulse amplifier ”, *Opt. Lett.* **23**,
1915 (1998).
17. J. Kunde, B. Baumann, S. Arlt, F. Morier-Genoud, U. Siegner, and U. Keller,
“Adaptive feedback control of ultra-fast semiconductor nonlinearities,” *Appl.*
Phys. Lett. **77**, 924 (2000).
18. M. M. Wefers and K. A. Nelson, “Analysis of programmable ultrashort waveform
generation using liquid-crystal spatial light modulator,” *J. Opt. Soc. Am. B* **12**,
1343-1362 (1995).
19. A. M. Weiner, “Femtosecond pulse shaping using spatial light modulators,” *Rev.*
Sci. Instrum. **71**, 1929–1960 (2000).
20. U. Keller, “Recent developments in compact ultrafast lasers”, *Nature* **424**,
831-838 (2003).
21. D. Kopt, G. Zhang, R. Fluck, M. Moser, and U. Keller, “All-in-one
dispersion-compensating saturable absorber mirror for compact femtosecond laser
sources,” *Opt. Lett.* **21**, 486-488 (1996).
22. *Frequency-Resolved Optical Gating: The Measurement of Ultrashort Laser
Pulses*, Rick Trebino, ed. (Kluwer Academic Publishers, Boston, 2002).

23. J. Peatross, A. Rundquist, "Temporal decorrelation of short laser pulses", JOSAB, volume 15 (1998).
24. M. Hacker, G. Stobrawa, T. Feurer, volume 9, "Iterative Fourier transform algorithm for phase-only pulse shaping", OPTICS EXPRESS (2001).
25. Ansy Rundquist, Anatoly Efimov and Dacid H. Reitze, "Pulse shaping with the Gerchberg-Saxton algorithm" , JOSAB, volume 19 (2002).
26. Y. Barad, H. Eisenberg, M. Horowitz and Y.Silberberg, "*Nonlinear Scanning Laser Microscopy by Third Harmonic Generation*", Appl. Phys. Lett. 70, 922 (1997).
27. D. Yelin, Y. Silberberg, Y. Barad and J.S. Patel, "*Depth-resolved imaging of nematic liquid crystals by third-harmonic microscopy*", Appl. Phys. Lett. 74, 3107 (1999).
28. J. W. P. Hsu, F. F. Schrey, and H. M. Ng, "Spatial distribution of yellow luminescence related deep levels in GaN", Appl. Phys. Lett. 83, 4172 (2003).
29. Nirit Dudovick, Barak Dayan, Sarah M. Fallagher Faeder, and Yaron Silberberg, "Transform-Limited Pulses Are Not Optimal for Resonant Multiphoto Transitions", Phys. Re. Lett. 86, 47 (2001).



30. Doron Meshulach and Yaron Silberberg, “Coherent quantum control of multiphoton transitions by shaped ultrashort optical pulses”, *Phys. Rev. A* 60, 1287 (1999).
31. N. Moriya, I. Brener, “Annealing of Cd-implanted GaAs: Defect removal, lattice site occupation, and electrical activation”, *J. Appl. Phys.* 73, 4248 (1993).
32. Yoshinori Takeuchi, Yunosuke Makita, “Observation of new common emissions in GaAs produced by ion implantation of four acceptor impurities”, *Appl. Phys. Lett.* 78, 59 (1986).

